Phase separation of +TIP-networks regulates microtubule dynamics

Julie Miesch[1#], Robert T. Wimbish[1#], Marie-Claire Velluz[1], Charlotte Aumeier[1,2]*

[1]Department of Biochemistry, University of Geneva, 1211 Geneva, Switzerland
[2]National Center for Competence in Research Chemical Biology, University of Geneva, 1211 Geneva, Switzerland
[#] equal contribution

*Correspondence to: Charlotte.aumeier@unige.ch

SUMMARY

Regulation of microtubule dynamics is essential for diverse cellular functions, and proteins that bind to dynamic microtubule ends can regulate network dynamics. Here we show that two conserved microtubule end-binding proteins, CLIP-170 and EB3, undergo phase separation and form dense liquid-networks. When CLIP-170 and EB3 act together the multivalency of the network increases, which synergistically increases the amount of protein in the dense phase. *In vitro* and in cells these liquid networks can condense tubulin. *In vitro* in the presence of microtubules, EB3/CLIP-170 phase separation can co-condense tubulin all along the microtubule. At this condition microtubule growth speed increases up to two-fold and depolymerization events are strongly reduced, compared to conditions with phase separation deficient networks. Our data show that phase separated EB3/CLIP-170 networks impact microtubule growth dynamics beyond direct protein-microtubule interactions.

Keywords: Microtubule, CLIP-170, EB3, microtubule dynamics, tubulin condensation, *in vitro*, liquid-liquid phase separation

Introduction

The microtubule cytoskeleton engages in a plethora of cellular processes, from organelle transport to cell division. To do so, the network dynamically modifies its structure in response to external cues and adapts its architecture to specific cellular functions. Microtubules themselves are highly dynamic polymers that can rapidly cycle between phases of polymerization and depolymerization, a characteristic which is critical for cytoskeletal re-organization (reviewed in Brouhard and Rice, 2018). In cells, microtubules polymerize at their plus-end by addition of GTP-tubulin. After GTP-tubulin addition, GTP is gradually hydrolyzed, resulting in a GDP-tubulin shaft behind the tip. Once the stabilizing GTP-tubulin "cap" disappears from the plus-end, the microtubule switches from growing to shrinking, an event termed catastrophe (Howard and Hyman, 2009; Brouhard et al., 2015; Gudimchuk and McIntosh, 2021). Conversely, microtubules can stop shrinking and switch to regrowth, an event termed rescue. The balance between growth and shrinkage is

intimately linked to the addition of free tubulin to the growing microtubule (Walker et al., 1988; Voter et al., 1991).

In addition to these intrinsic modes of regulation, microtubule dynamics can be fine-tuned by Plus Tip-Interacting Proteins (+TIPs) (reviewed in Akhmanova and Steinmetz, 2010). +TIPs are functionally independent and structurally diverse microtubule regulators that concentrate at growing microtubule ends while exhibiting a weak affinity for the microtubule shaft. It is generally accepted that the unique localization of +TIPs at microtubule ends results from their specific binding to the GTP-tubulin cap (Akhmanova and Steinmetz, 2015).

Key integrators of +TIP-networks are the End-Binding proteins (EBs), as they autonomously bind to GTP-tubulin at growing microtubule ends and recruit a battery of non-autonomously binding +TIPs (reviewed in Galjart, 2010). Within the EB family, higher eukaryotes express three proteins termed EB1, EB2, and EB3. These proteins increase microtubule plus-end dynamics by promoting catastrophes and increasing growth speed *in vitro* (Bieling et al., 2008; Vitre et al., 2008; Komorova et al., 2009; Montenegro Gouveia et al., 2010).

A key accessory protein recruited to plus ends by the EBs is the Cytoplasmic Linker Protein of 170 kDa (CLIP-170), which increases microtubule rescue frequency and growth speeds (Perez et al., 1999; Arnal et al., 2004; Bieling et al., 2007; Bieling et al., 2008; Komorova et al., 2002, 2005). CLIP-170 consists of a microtubule binding "head" domain in its N-terminus, followed by a central coiled-coil region and a zinc-knuckle domain, hereafter referred to as the "C-terminal region" (Pierre et al., 1992; Pierre et al., 1994; Diamantopolous et al., 1999). Most studies of CLIP-170 function *in vitro* have focused on truncated versions, containing only the monomeric head domain (H1) or the head domain with a small extension that allows dimerization (H2) (Figure 1A); thus, it is unclear how full-length CLIP-170 contributes to microtubule dynamics.

Early studies of CLIP-170 expression in cells revealed that in addition to its microtubule plus-end localization, it also formed cytoplasmic "patches" that co-localized with EB1 and the dynein-activating protein dynactin (Pierre et al., 1994; Goodson et al., 2003). Based on the physical properties of these CLIP-170 patches, it has recently been suggested that they form by liquid-liquid phase separation (LLPS) (Wu et al., 2021; Jijumon et al., 2022).

LLPS is the process by which molecules spontaneously condense into droplets and de-mix from their surrounding solution, resulting in the co-existence of two unique liquid phases (reviewed in Boeynaems et al., 2018; Hyman et al., 2014; Shin and Brangwynne, 2017). Recently, LLPS has been implicated in driving microtubule-related processes, including spindle assembly (Jiang et al., 2015), nucleation of acentrosomal and branched microtubules (Hernández-Vega et al., 2017; King and Petry, 2020), and centrosome maturation (Woodruff et al., 2017; Jiang et al., 2021). A key shared feature of these processes is the co-condensation of tubulin with LLPS-potent microtubule-

associated proteins to catalyze biochemical reactions. Along these lines, condensation of a microtubule +TIP-network has been proposed based on transient multivalent interactions between the +TIPs (Akhmanova and Steinmetz, 2015; Wu et al., 2021). Despite this, LLPS of +TIPs and its function is still unclear.

+TIPs concentrate at the growing GTP-microtubule tip. A combination of *in vivo, in vitro* and *in silico* work has indicated that the GTP-tubulin cap size is 1-60 tubulin layers, indicating a length of < 500 nm (Voter et al., 1991; Walker et al., 1988; Drechsel and Kirschner, 1994; Schek et al., 2007, Seeptapun et al. 2012; Rickman et al., 2017). Puzzlingly, in cells +TIP networks bind to a region at the microtubule end up to 4-fold longer than this, with network lengths up to 2 µm (Komarova et al. 2009; Seepatun et al., 2012; Roth et al. 2019). The discrepancies between +TIP network profiles *in vitro* and in cells could be due to different sizes of the GTP-cap, but also prompts the question of whether network densities and organizational properties could impact network extension.

Interestingly, overexpressed EB3 and CLIP-170 exhibit atypical network formation at the growing microtubule tip. Both proteins leave trailing protein "foci" behind the leading network edge (Mustyatsa et al., 2019; Henrie et al., 2020, Komarova et al. 2009, Nakamura et al. 2012, Mohan et al., 2013). One explanation for these foci is that they form by binding to tubulin remaining in the GTP-state behind the GTP-cap (Perez et al., 1999; de Forges et al., 2016; Henrie et al., 2020). As overexpressed CLIP-170 has the potential to undergo LLPS (Wu et al., 2021; Jijumon et al., 2022), another possibility would be that CLIP-170 foci split off from the leading network in a process resembling fission of condensates.

In this study, we use tandem in-cell and *in vitro* approaches to investigate +TIP condensation and their function. We provide evidence that +TIP networks in cells may have liquid properties. We demonstrate that the +TIPs EB3 and CLIP-170 undergo LLPS at nanomolar concentrations in the absence of crowding agents. The EB3 and CLIP-170-containing droplets co-condense tubulin, and depend on protein regions promoting multivalent interactions. In the presence of microtubules, EB3/CLIP-170 promote rapid growth speeds while reducing catastrophe and pausing frequencies at the microtubule plus-end. Taken together, our results suggest a mechanism whereby +TIP LLPS plays a role in regulating microtubule dynamics.

Results

+TIP-networks exhibit properties reminiscent of phase separation

We first studied if +TIP-network profiles with trailing protein foci could result from LLPS, by overexpressing GFP-CLIP-170 in RPE-1 cells. Analysis of plus-end fluorescence intensity profiles in cells revealed that 80 % of the GFP-CLIP-170 networks left behind foci (Figures 1B and C). Dynamic analysis of CLIP-170 networks showed that the remaining protein foci bound to the microtubule shaft dissolved over time (Figure 1D and Movie 1). We next probed the material

properties of +TIP-networks by treating cells with the aliphatic alcohol 1,6-hexanediol to reduce hydrophobic interactions (Kroschwald et al., 2017). While untreated cells exhibited 3 µm long +TIP-networks, upon hexanediol treatment, the profile of the +TIP-network reduced to ~1.5 µm foci (Figures S1A, B and Movie 2), indicating that hydrophobic interactions influence +TIP network organization.

To rule out that the observed foci formation is not an artefact of overexpression, we measured plus-end fluorescence intensity profiles of endogenous CLIP-170. In line with overexpression studies, we observed that for endogenous CLIP-170, ~70% of the +TIP-networks had foci (Figures 1B and C). EB3, another prominent +TIP, followed a comparable fluorescence profile, with ~75% of the endogenous EB3 networks having foci (Figures 1B and C), consistent with an overexpression-based study (Mustyatsa et al., 2019). Co-staining of EB3 and CLIP-170 revealed that most networks displayed fluorescence profiles with distinct EB3 and CLIP-170 foci co-localization (Figure 1F).

When we overexpressed the CLIP-170 truncated H2- and H1-mutants (Figure 1A), both tracked the growing GTP-microtubule tip, as previously reported (Figure 1E) (Komarova et al., 2002; Folker et al., 2005). However, the presence of foci behind the leading edge of the H2- and H1-networks was dramatically reduced compared to CLIP-170 (Figure 1C). This suggests that the C-terminal region of CLIP-170 influences network organization at microtubule ends. Since H1 and H2 retain binding to the growing GTP-tip, this result implies that foci formation cannot be solely explained by the presence of GTP-islands in the shaft and might also result from material properties of the multivalent +TIP-network.

CLIP-170 forms biomolecular condensates in cells

Analysis of +TIP-network fluorescence intensity revealed that with increasing GFP-CLIP-170 expression levels, the CLIP-170 concentration plateaued in +TIP-networks, after an initial increase (Figures 2A and B). This indicates that CLIP-170 in +TIP-networks reaches a state of saturation and suggests a defined stoichiometry of CLIP-170 with the network. Interestingly, at the onset of this transition CLIP-170 patch formed in the cytoplasm (Figures 2A and B). Indeed, overexpression of CLIP-170 in CRISPR/Cas9 knock-in GFP-tubulin RPE-1 cells resulted in cytosolic CLIP-170 patches which displayed liquid properties, undergoing fusion and fission within 5 sec (Figure 2C and Movies 3, 4). Fluorescence recovery after photobleaching (FRAP) revealed that CLIP-170 diffuses highly within these patches and showed a high protein exchange rate with the pool outside the patch, with a recovery half-life and mobile fraction of 27.5 seconds and 93 ± 32 %, respectively (Figure 2D and Movie 5). These properties lead us to conclude that CLIP-170 patches are biomolecular condensates in cells, hereafter called droplets.

CLIP-170 forms biomolecular condensates in vitro

137 To address whether CLIP-170 alone undergoes phase separation, we purified recombinant full-
138 length human GFP-CLIP-170 (FL-CLIP) from insect cells (Figure S3A) and reconstituted its phase
139 separation properties *in vitro*. In the absence of crowding agents and at physiological salt
140 concentrations, FL-CLIP robustly condensed into spheres at concentrations as low as 3.1 nM
141 (Figures 2E and S3B), which is below the cellular concentration of ~110 nM (Wisniewski et al.,
142 2014). To estimate the amount of FL-CLIP in the dense phase, we used a high throughput confocal
143 microscopy-based approach. Briefly, i) protein mixtures were incubated in 384-well plates, ii)
144 proteins in the dense phase were centrifuged onto the bottom of the wells, iii) wells were imaged
145 using an automated confocal microscope, and iv) surface coverage of protein in the dense phase
146 on well-bottoms was measured (Figure S3C; see Methods for details). A hallmark property of
147 LLPS-potent proteins is that they condense in a concentration-dependent manner and in response
148 to the presence of crowding agents (Alberti et al., 2019). In line with this, the sphere size and
149 amount of FL-CLIP in the dense phase increased in a concentration-dependent manner even in the
150 absence of crowding agents (Figures 2F and S3D). Increasing the ionic strength of the buffer
151 reduced the sphere size (Figure S3B). Addition of a crowding agent, 2 % polyethylene glycol
152 (PEG), increased the amount of FL-CLIP in the dense phase by 1.5-fold but reduced sphere size
153 (Figures S3E and F).
154
155 In line with the case in cells, FL-CLIP spheres displayed liquid properties such as fusion, although
156 5-times slower than what we observed in cells (Figure 2G and Movie 6). We further interrogated
157 the liquid properties of these spheres by FRAP, which confirmed that FL-CLIP diffuses within the
158 spheres with a half-life of 27.5 s, identical to the recovery speed in cells. However, FL-CLIP
159 exchange dynamics were reduced three-fold with a mobile fraction of 28 ± 12% (Figure 2H and
160 Movie 7). By calibrating the fluorescent intensity of GFP, we estimated that the initial FL-CLIP
161 concentration increased 8.5-fold within these spheres (Table 1). Collectively, these results show
162 that FL-CLIP undergoes LLPS and forms droplets *in vitro* at nanomolar concentration and in the
163 absence of further proteins or crowding agents. We hypothesize that the discrepancies between the
164 material properties of the droplets in cells and *in vitro* are due to the presence of additional proteins
165 and/or CLIP-170 post-translational modifications in the cell droplets.
166
167 *The CLIP-170 C-terminal region drives CLIP-170 into the dense phase*
168 We next investigated which domains of CLIP-170 drive droplet formation. We expressed GFP-
169 tagged H2- and H1-CLIP mutants in RPE-1 cells where the C-terminal region is truncated or fully
170 removed (Figure 1A) (Pierre et al., 1992, 1994; Diamantopoulos et al., 1999; Goodson et al., 2003).
171 In line with previous observations, we saw that H1 and H2 displayed microtubule plus-end tracking
172 activity in cells, but did not form any cytosolic droplets even at high expression levels (Figure 3A
173 and Movies 8, 9) (Pierre et al., 1994; Goodson et al., 2003). To understand to which extent the C-
174 terminal region is necessary for CLIP-170 to undergo LLPS, we purified recombinant human H1
175 and H2 from bacteria and measured their ability to condense *in vitro* at nanomolar concentrations
176 (Figure S4A). While FL-CLIP phase separated in the absence of other factors, H1 showed faint

177 irregular-shaped aggregation but no droplet formation, even in presence of 10 % PEG (Figures 3B,
178 C and S4B, C). In contrast to the case in cells, at nanomolar concentration H2 underwent
179 condensation *in vitro*, although with a 300-fold reduction of protein surface coverage and a 25-
180 fold reduction in droplet size compared to FL-CLIP (Figures 3B, C, D and S4A). Addition of 2 %
181 PEG increased H2 condensate formation by 3-fold but did not affect condensate size (Figures 3B,
182 C and S4B, C).
183
184 Intrinsically disordered domains are common features of proteins that undergo LLPS (Boeynaems
185 et al., 2018). To parse out the contributions of disordered domains to FL-CLIP's phase separation
186 potency, we engineered a mutant containing the H2 domain fused to the far C-terminal region,
187 termed H2-tail (Figure S4E). This mutant lacks the majority of the coiled-coil region but retains
188 many predicted disordered regions within CLIP-170 (Figure S4E). Attempts to purify this mutant
189 resulted in insoluble large protein aggregates, highlighting the importance of the coiled-coil region
190 for CLIP-170's solubility (Figure 3B). Collectively, these results show that while the monomeric
191 H1 is sufficient to track the growing microtubule tip, the dimeric form of CLIP-170 is necessary
192 to undergo LLPS and that the C-terminal region robustly drives CLIP-170 condensation.
193
194 *EB3 undergoes LLPS and co-condenses with CLIP-170*
195 CLIP-170 requires the presence of EBs to localize to growing microtubule ends (Dixit et al., 2009,
196 Bieling et al., 2008). This prompted us to ask whether purified FL-CLIP and EB3 could co-
197 condense *in vitro*. We first studied EB3 alone and observed that it has the capacity to undergo
198 LLPS at micromolar concentrations: compared to 48 ± 17 μm^2 large droplets observed for 400 nM
199 FL-CLIP, at 1 μM EB3 phase separated into many small 1.9 ± 0.6 μm^2 droplets, resulting in a 3.5-
200 fold reduced surface coverage (Figures 4A, B and S5A). EB3 fraction in the dense phase was
201 comparable between 0 and 2 % PEG (Figures 4A and B). FRAP revealed that EB3 diffused within
202 these patches at the same rate as FL-CLIP, but had a 2.5-fold higher protein exchange rate with
203 the pool outside the droplet (Figure 4C and Movie 10).
204
205 We next tested the ability of CLIP-170 to co-condense with EB3. Indeed, FL-CLIP and EB3
206 robustly co-condensed into droplets, in which both proteins showed a homogenous distribution
207 (Figure 4D and S5B). To address if diffusion kinetics are impacted by a multivalent EB3/FL-CLIP-
208 network, we repeated our FRAP experiment. Surprisingly, the time to recover after photobleaching
209 was the same for EB3, FL-CLIP and EB3/FL-CLIP droplets (Movies 7, 10, 11 and Figures 2H,
210 4C and S5C). The mobile fraction of FL-CLIP and EB3/FL-CLIP was also comparable, however
211 EB3 droplets had a 2- fold higher mobile fraction. This indicates that fluorescent recovery of FL-
212 CLIP and EB3/FL-CLIP droplets depends more on protein diffusion, while protein exchange with
213 the soluble pool further impacts recovery of EB3 droplets. In line with this observation, the three
214 different droplets exhibited distinct surface interaction properties: EB3 did wet the coverslip
215 resulting in flat droplets, while FL-CLIP and EB3/FL-CLIP droplets remained a similar sphere-
216 like shape when bound to the coverslip (Movie 12, 13 and 14). Co-condensation of EB3 with FL-

217 CLIP increased the number of small droplets, such that droplets larger than 40 μm^2 were rarely
218 observed (Figures S5D). This reduced the average droplet size by 20-fold compared to FL-CLIP,
219 despite a 6-fold increase in total protein concentration in the solution (2 μM to 12 μM) (Figure
220 S5E). These results show that EB3 and FL-CLIP can co-condensate and that the multivalency of
221 the network does not further impact FL-CLIP diffusion within the network, while droplet size and
222 surface tension can be impacted by the protein composition.
223
224 To study whether partitioning of +TIPs into pre-formed droplets affected condensation properties,
225 we compared: i) co-condensation of EB3 and FL-CLIP, ii)) addition of FL-CLIP to pre-formed
226 EB3 droplets and iii) addition of EB3 to pre-formed FL-CLIP droplets. Addition of FL-CLIP to
227 EB3 droplets increased the droplet size over time; however, upon reaching coarsy steady state, we
228 observed no differences in droplet size or protein concentrations within the droplets between the
229 three conditions (Figure 4D).
230
231 Interactions between EB1 and CLIP-170 are driven by the last C-terminal tyrosine of EB1 (Bieling
232 et al., 2008). To probe whether specific protein-protein interactions underlie EB3/FL-CLIP co-
233 condensation, we purified a EB3 tyrosine deletion mutant (EB3-ΔY) and repeated our
234 colocalization assay. Removal of the last tyrosine drastically reduced EB3's ability to co-condense
235 with FL-CLIP (Figure 4E), despite leaving EB3-ΔY's intrinsic phase separation properties intact
236 (Figure S5F). Thus, specific binding interactions between EB3 and FL-CLIP are key features in
237 their ability to co-condense. Altogether, these data show that EB3 undergoes phase separation and
238 can co-condense with FL-CLIP into droplets with homogenous protein distribution. These droplets
239 exhibit similar fluid properties, but likely different surface interaction properties.
240
241 *EB3/CLIP-170-networks cooperatively phase separate*
242 Given that EB3/FL-CLIP droplets were reduced in size, we quantified whether the total amount of
243 protein in the dense phase is reduced. Measuring the concentration of FL-CLIP in droplets
244 compared to the dilute phase showed that FL-CLIP is enriched 24-fold in the droplet (Table 1).
245 Co-condensation of FL-CLIP and EB3 only slightly increased the concentration of FL-CLIP in the
246 droplet, while condensation of EB3 was increased 1.4-fold (Table 1). This implies, that FL-CLIP
247 drives the partitioning of EB3 into droplets. To probe this observation further and to analyze the
248 total amount of protein in the diluted and dense phase, we performed a droplet-pelleting assay
249 followed by SDS-PAGE analysis (for details see Methods). Similar to what we observed by
250 microscopy, in EB3/FL-CLIP networks the amount of condensed EB3 increased by 1.7-fold
251 compared to amounts measured for EB3 alone (Figures 5A and B). We further studied the
252 synergistic effect on droplet formation with our high-throughput microscopy assay. Although the
253 size of EB3/FL-CLIP droplets decreased, the number of droplets increased leading to a surface
254 coverage 2.5-fold higher than FL-CLIP droplets alone (Figure 5C, D and S5E). This resulted in a
255 40 % increase of surface coverage by EB3/FL-CLIP networks when compared to the sum of the
256 surface coverages of EB3 alone plus FL-CLIP alone (Figure 5E).

257
258 Repeating the EB3 experiment with H2 reduced surface coverage by 1.5-fold compared to the
259 presence of FL-CLIP, and H1 further decreased surface coverage by 2.5-fold (Figures 5F and
260 S5G). These data demonstrate that CLIP's C-terminal region is essential for a highly multivalent
261 EB3/FL-CLIP network formation. We further show that EB3 and CLIP-170 can undergo LLPS
262 both independently, and that when acting as an ensemble, the amount of proteins in the dense phase
263 synergistically increases.
264
265 *CLIP-170 and EB3 condense tubulin in vitro*
266 A CLIP-170 dimer has as many as 8 tubulin binding sites, can bind tubulin *in vitro,* and colocalizes
267 with tubulin in cells (Figure 6A) (Pierre et al., 1994 et al., 1999; Perez et al., 1999; Gupta et al.,
268 2010). We therefore asked if CLIP-170 droplets can co-condense tubulin *in vitro*. Tubulin alone
269 did not form droplets at micromolar concentrations; even in the presence of 5% PEG only
270 aggregation was observed (Figure S6A). However, when 200 nM FL-CLIP was mixed with 400
271 nM Atto565-tubulin, the two proteins phase separated into 26.8 ± 12 μm^2 droplets (Figures 6B and
272 S6B). We repeated these experiments with H1 and found irregular-shaped aggregation with tubulin
273 but no droplet formation (Figure 6B). Based on the intrinsic phase separating capacity of EB3, we
274 studied whether EB3 alone could condense tubulin (Figure 4A). Indeed, EB3 also co-condensed
275 tubulin, although into much smaller 1 ± 0.07 μm^2 droplets, in line with our observed EB3 droplet
276 size distribution (Figures 6C and S6C). EB3/FL-CLIP networks also condensed tubulin into
277 intermediate-sized droplets, consistent with EB3 reducing the droplet size compared to FL-CLIP
278 (Figure S6C). These results demonstrate that FL-CLIP, EB3 and EB3/FL-CLIP networks are
279 potent to condense tubulin.
280
281 Although all three different protein droplets condensed tubulin, the distribution of tubulin differed.
282 Tubulin was homogenously mixed within FL-CLIP droplets and in addition formed a shell-like
283 structure around the droplets (Figure S6D). Within the shell, tubulin was concentrated twice as
284 high as within the droplet (Table 1). This result indicates that within the droplet tubulin is mixed
285 with FL-CLIP, while tubulin phase separates at the solution interface. In contrast to FL-CLIP
286 droplets, tubulin was homogenously distributed in EB3 and EB3/FL-CLIP droplets (Figure S6D).
287 This implies that addition of EB3 changes the surface properties such that tubulin condensation at
288 the interphase is not favorable.
289
290 Strikingly, FL-CLIP droplets enriched condensed tubulin 40-fold more than EB3 droplets, even at
291 5-fold lower FL-CLIP concentrations (Figure 6C). This difference in condensed tubulin cannot be
292 solely explained by the 3.5-fold difference in surface coverage between EB3 and FL-CLIP, but
293 indicates a different in the potency of the two proteins to condense tubulin (Figure 6C). Based on
294 this result, we asked whether addition of EB3 to FL-CLIP impacts tubulin condensation. Indeed,
295 we observed that EB3/FL-CLIP networks condensed tubulin 4-fold less efficient than FL-CLIP
296 alone (Figure 6C). We hypothesize that within a multivalent tubulin/EB3/FL-CLIP network the

297 heterotypic interaction between EB3 and FL-CLIP are stronger than EB3-tubulin and FL-CLIP-
298 tubulin interactions, leading to a reduction of tubulin condensation, especially around the droplets.
299 Collectively, these results show that FL-CLIP can condense tubulin effectively and that EB3
300 reduces the tubulin condensation capacity of FL-CLIP droplets, while changing the surface
301 properties of the droplets.
302
303 *Tubulin co-condenses with CLIP-170 in cells*
304 We next addressed whether CLIP-170 can condense tubulin in cells. Overexpressing GFP-CLIP-
305 170 in RPE-1 cells revealed that CLIP-170 droplets colocalized with areas of high tubulin
306 fluorescence intensity (Figure 6D, top panel) (Perez et al., 1999). However, it was not possible to
307 distinguish if these areas corresponded to microtubule bundles, or if the local increased signal
308 resulted from tubulin condensation. To address this question, we depolymerized the microtubule
309 network with 5 µM nocodazole. After microtubule depolymerization, tubulin showed robust co-
310 localization with CLIP-170 droplets (Figure 6D, middle panel), and tubulin fluorescence intensity
311 was 2.4-fold higher in the droplets compared to the cytoplasm (Figure 6E). To study whether
312 CLIP-170 could also co-condense tubulin at endogenous concentration, we used antibody staining
313 after microtubule network depolymerization. In WT cells, small foci of endogenous CLIP-170
314 were frequently observed after microtubule network depolymerization, and these foci showed local
315 enrichment of tubulin (Figure 6D, bottom panel). In cells depleted of CLIP-170 and in CLIP-170
316 knockdown cells rescued with H2, we did not observe tubulin/FL-CLIP foci (Figure S6E).
317 Contrary to our *in vitro* experiments, tubulin foci were not observed in nocodazole-treated cells
318 overexpressing H2 or EB3 (Figure S6F). After depolymerization of the microtubule network EB3
319 was cytoplasmic with a few small foci, but showed no distinct co-condensation with tubulin
320 (Figure S6F). We conclude that CLIP-170, but not EB3, can condense tubulin in cells.
321
322 *Phase separation-potent +TIP networks increase microtubule growth*
323 The absence of either EB3 or CLIP-170 at the microtubule tip does not reduce growth speeds in
324 cells (Komorova et al., 2002; Straube et al., 2007; Komorova et al., 2009). However, combined
325 siRNA knockdown of EB3 and CLIP-170 reduced microtubule growth speeds by 20 % (Figures
326 S7C and D). To understand if LLPS of +TIPs could impact microtubule tip dynamics, we turned
327 to *in vitro* reconstitution. We first reconstituted microtubule growth in presence of +TIP-networks
328 with either reduced (50 nM H2 + 800 nM EB3) or minimal (50 nM H1 + 800 nM EB3) LLPS
329 activity (Figure 5F), implying reduced or minimal co-condensation of tubulin at the growing tip
330 (Figure 6C). To our knowledge these CLIP mutants preserve all binding domains to interact with
331 EB3 and tubulin, implying that the difference between these networks lies primarily in their phase
332 separation potency. As observed previously, EB3 alone increased microtubule growth speeds by
333 1.5-fold and catastrophe frequency by 8-fold (Figures 7A and B) (Komorova et al., 2009;
334 Montenegro Gouveia et al., 2010). Addition of H1 or H2 to the assay with EB3 resulted in tip-
335 tracking behavior by EB3/H1 and EB3/H2 networks, but did not further change any of the dynamic
336 parameters compared to EB3 alone (Figures 7A, B and S8A). These results show that CLIP/EB3

337 networks with reduced or minimal capacity to condense tubulin have the same impact on
338 microtubule tip dynamics as EB3 alone.
339
340 When we repeated the reconstitution experiments with EB3/FL-CLIP, microtubules grew at a
341 speed of 3.5 µm/min, a 1.5-fold increase compared to analogous experiments with EB3/H2 and
342 EB3/H1, and nearly four-fold increase compared to controls with tubulin alone (Figures 7A, B and
343 Movie 15). Furthermore, catastrophe events were reduced under these conditions (Figures 7A and
344 B), and when they occurred were rapidly followed by rescue events (Figure S8A). To reconstitute
345 this fast microtubule growth in presence of a phase separation deficient EB3/H2 network, we
346 increased the tubulin concentration while keeping the EB3/H2 concentration constant. We
347 measured microtubule growth speeds and found that a growth speed of 3.5 µm/min (the speed
348 achieved by EB3/FL-CLIP in the presence of 5 µM tubulin) corresponds to 12.8 µM tubulin in
349 presence of EB3/H2 (Figures S8B and C). These results show that phase separation-potent
350 EB3/FL-CLIP networks increase the growth rate and reduce the catastrophe events compared to
351 EB3/H2 networks. A phase separated +TIP network might impact the growing microtubule tip due
352 to changes in material properties, or due to condensation of tubulin at the tip, based on our
353 observation that EB3/FL-CLIP can condense tubulin (Figure 6C).
354
355 *+TIPs undergo LLPS and condense tubulin on microtubules, promoting microtubule growth*
356 To understand if LLPS of EB3/FL-CLIP networks could enrich tubulin on microtubules, we used
357 microtubules as a platform to induce LLPS. A recent study showed that addition of cell lysate
358 containing overexpressed CLIP-170 to microtubules formed CLIP-170-containing droplets along
359 microtubules (Jijumon et al., 2022). We asked if this droplet formation is due to the crowding
360 environment of the cell lysate, or a general property of FL-CLIP. Under assay conditions with
361 lower ionic strength (see materials and methods), we repeated our assay from above to study if
362 purified EB3 together with FL-CLIP could phase separate along microtubules. When we incubated
363 purified CLIP-170 and EB3 with dynamic microtubules in vitro, we found that purified EB3/FL-
364 CLIP formed droplets along the shaft (Figure 7C and Movie 16).
365
366 In line with our observations that EB3/FL-CLIP droplets condensed tubulin (Figure S6D), these
367 networks enriched tubulin all along the microtubule and co-condensed tubulin over time into
368 droplets on the shaft, even more efficient than free floating droplets (Figures 7C-G). At this
369 condition where tubulin condensed along the microtubule, we observed rapid microtubule growth
370 speeds of 3.6 µm/min and very few catastrophe events or pauses in the growth phase (Figures 7D,
371 H and S8D). This increase in growth speed and reduction in catastrophe events is in line with our
372 results from above where EB3/FL-CLIP was located at the microtubule tip. When we repeated
373 these experiments with less potent phase separating EB3/H2-networks, we only occasionally
374 observed condensate formation along the microtubule (Figure 7D, left panel). In presence of
375 EB3/H2-networks growth speeds were 2-fold slower than for EB3/FL-CLIP, catastrophe
376 frequencies were increased 7-fold and pauses increased 30-fold (Figure 7H and S8D). In the

absence of EB3, we did not observe microtubule binding or increased growth speeds for any CLIP constructs (Figures S8E and F). Collectively, these experiments demonstrate that EB3/FL-CLIP networks undergo LLPS on microtubules, can condense tubulin, and drive microtubule growth.

Discussion

Rearrangements of the microtubule network architecture require spatiotemporal regulation of microtubule growth. A large body of work has highlighted the role of +TIPs that act as microtubule polymerases (such as XMAP215) or increase microtubule tip dynamics (such as the EBs) in promoting these highly regulated changes (Gard and Kirschner, 1987; Srayko et al., 2005; Straube and Merdes, 2007; Brouhard et al., 2008; Bieling et al., 2008; Vitre et al., 2008; Zanic et al., 2013; Yang et al., 2017). While these studies showed the impact of +TIPs on microtubule dynamics, it has remained unclear how these proteins self-assemble to form highly dynamic and multivalent networks. LLPS allows for network formation of proteins based on highly multivalent interactions. We now provide evidence that LLPS of +TIPs could be a mechanism to explain the formation of +TIP-networks at the growing microtubule tip. This mechanism could be a base to locally recruit and enrich diverse +TIPs.

LLPS of proteins is often driven through weak multivalent interactions and low complexity domains (Boeynaems et al., 2018). A growing body of evidence also implicates coiled-coil regions of proteins in driving their LLPS. Coiled-coil domains allow for rapid dimerization and self-oligomerization which might be sufficient for the assembly of certain condensates (Larson et al., 2017; Strom et al., 2017). Notably, coiled-coil containing proteins are highly enriched in phase-separated centrosomes and P-granules (Salisbury, 2003; Ford and Fioriti, 2020), and many of these proteins phase separate in a coiled-coil dependent manner (Mitria and Kriwacki, 2016; Woodruff et al., 2017; Jiang et al., 2021). Our experiments using CLIP-170 truncation mutants emphasize the role that coiled-coil proteins can play in driving LLPS. In addition, our data implies that specific binding domains between EB3 and FL-CLIP are needed to form a multivalent network, as deletion of one single tyrosine strongly reduces EB3 co-condensation with FL-CLIP.

Here, we propose a new mechanism by which LLPS of +TIPs regulate microtubule growth. Our model of LLPS-driven microtubule growth is based on the following observations: i) the +TIPs EB3 and CLIP-170 have the capacity to undergo LLPS *in vitro* and in cells (Figures 2-5), ii) phase separated EB3/FL-CLIP droplets can condense tubulin (Figure 6), iii) microtubule growth speed is increased and catastrophe frequency reduced when EB3/FL-CLIP undergo phase separation on microtubules (Figure 7H), and iv) tubulin condensed along the microtubule in presence of phase separated EB3/FL-CLIP (Figure 7C-G). We hypothesize that this tubulin enrichment may be a mechanism to increase local tubulin availability at microtubule ends uncoupled from cytoplasmic tubulin concentrations. Microtubule dynamics might be further modulated by the viscosity of the droplets, such as sterically constraining protofilaments in a manner that accelerates growth or prevents catastrophes.

417
418 Microtubules could serve as a general platform to concentrate proteins locally to a LLPS-sufficient
419 concentration. We hypothesize that the mechanism of LLPS initiation at the growing tip depends
420 on conformational properties of the growing microtubule tip, which leads to differential binding
421 of EB3 to the tip over the shaft (Zhang et al., 2015) and subsequent recruitment of CLIP-170 to
422 form a multivalent network. As LLPS is a concentration dependent process, the local recruitment
423 of EB3 and CLIP-170 could increase their concentration compared to the solution to such an extent
424 that they undergo LLPS. We hypothesize that, upon reaching a critical CLIP-170 concentration,
425 the +TIP-network undergoes LLPS. This +TIP-droplet has then the potential to, e.g. co-condenses
426 tubulin, and drive microtubule growth. Once the GTP-cap is hydrolyzed, the +TIP-droplet
427 dissolves. This implies that the shape of the +TIP-droplets would follow the decaying GTP-tubulin
428 profile at the growing microtubule tip. Whether the stoichiometry between EB3 and CLIP-170 has
429 an impact on the LLPS process, as well as the distinct fluid properties and dynamics of an
430 EB3/CLIP-170 droplet, merit investigation in future work.
431
432 A EB3/FL-CLIP droplet has distinct surface properties that differ from EB3- or FL-CLIP droplets
433 in: surface tension, mobile fraction and tubulin interaction. These characteristics might be
434 important for microtubule - EB3/FL-CLIP droplet interaction. Interestingly, we observed that
435 EB3/FL-CLIP droplets on microtubules strongly enriched tubulin, while tubulin was less
436 condensed in free floating EB3/FL-CLIP droplets. This might indicate that the microtubule surface
437 can change the propensity of the EB3/FL-CLIP droplets to condense tubulin.
438
439 We hypothesize that LLPS of +TIPs serves an organizational purpose, allowing for the formation
440 of a highly concentrated protein network at microtubule ends. Based on our observation that +TIPs
441 concentrate soluble tubulin into droplets and on microtubules, we postulate that this process may
442 contribute to regulation of microtubule dynamics in cells. Interestingly, depletion of CLIP-170 or
443 EB3 from cells has been reported to only mildly affect microtubule dynamics in cells (Komorova
444 et al., 2002), while depletion of EB3 and CLIP-170 reduced the growth speed by 20 % (Figure S7)
445 Given that there is a level of redundancy in the functions of EBs in regulating microtubule
446 dynamics in cells (Komorova et al., 2009; Yang et al., 2017), and the observation that diverse
447 +TIPs partition into CLIP-170 condensates (Wu et al., 2021), we favor the hypothesis that +TIP-
448 network condensation can be driven by multiple different proteins. In this scenario, individual
449 depletions of CLIP-170 or EB3 would not strongly diminish microtubule growth, as other +TIPs
450 could compensate for driving +TIP-network phase separation. Further studies comparing the
451 phase-separation potencies of other +TIPs, as well as combinatorial depletions of LLPS-potent
452 +TIPs in cells, will be of interest in addressing this question.
453
454 Is phase separation a common feature of +TIPs? Studies performed in parallel to our work show
455 that this phenomenon is conserved across evolution: +TIPs in budding yeast, fission yeast, and
456 higher eukaryotes have recently been demonstrated to undergo phase separation (Maan et al., 2021;

457 Meier et al., 2021; Song et al., 2021, Jijumon et al., 2022). Intriguingly, in line with our results,
458 the yeast studies confirmed that the CLIP-170 homolog played a key role in the phase separation
459 process, whereas LLPS potency of EB homologs varied between organisms. The role of different
460 mammalian EB family members in regulating LLPS will be an interesting direction for future
461 studies. The ability of +TIP-networks to phase separate depends on intrinsically disordered regions
462 (Maan et al., 2021; Song et al., 2021) and multivalent interaction modules (Meier et al., 2021),
463 consistent with the observation that these features are highly evolutionarily conserved across
464 +TIPs (Wu et al., 2021). Further studies will be necessary to investigate whether additional +TIPs
465 contribute to the formation and regulation of +TIP-droplets.
466
467 Our work here and recent studies demonstrate that +TIP networks can behave like liquid
468 condensates (Wu et al., 2021; Maan et al., 2021; Meier et al., 2021; Jijumon et al., 2022; Song et
469 al., 2021). This work adds to the growing list of microtubule-related processes that are driven by
470 LLPS and provides an exciting new paradigm for how cells can spatiotemporally control
471 microtubule dynamics through local tubulin concentration (Jiang et al., 2015; Woodruff et al.,
472 2017; Hernández-Vega et al., 2017; King and Petry, 2020; Jiang et al., 2021; Maan et al., 2021;
473 Meier et al., 2021; Song et al., 2021). Interrogating the mechanical properties and composition of
474 +TIP-droplets, as well as studying their regulation throughout the cell cycle, will be exciting
475 avenues for future research.
476
477 **Acknowledgements**
478 We thank Thomas Surrey (Centre for Genomic Regulation, Barcelona, Spain) for providing the
479 FL-CLIP-170 expression vector for insect cells, and Michel Steinmetz (Paul Scherrer Institute,
480 Villigen PSI, Switzerland) for providing vectors for EB3 purification. We would also like to thank
481 Peter Bieling (Max Planck Institute of Molecular Physiology, Dortmund, Germany) for helpful
482 discussions regarding expression and purification of FL-CLIP-170, and Maria Hondele
483 (University of Basel, Switzerland) for helpful discussions for phase separation experiments. We
484 would like to thank Dimitri Moreau and Stefania Vossio from the ACCESS Geneva high-content
485 microscopy facility for help with microscopy and data analysis. We also thank Oscar Vadas and
486 Rémy Visentin of the Protein Platform (Faculty of Medicine, University of Geneva, Switzerland)
487 for support in FL-CLIP-170 expression. We would also like to thank Karsten Kruse and Marcos
488 Gaitan-Gonzales and for critically reading the manuscript.
489
490 JM has been supported by the SNSF, 31003A_182473; RTW has been supported by the NCCR
491 Chemical Biology program; CA has been supported by the DIP of the Canton of Geneva, SNSF
492 (31003A_182473), and the NCCR Chemical Biology program.
493
494 **Author Contributions:** JM and RTW performed and designed the experiments with the help of
495 CA. MCV purified the proteins. JM, RTW, and CA analyzed data. RTW and CA wrote the
496 manuscript.

Declaration of Interests: The authors declare no competing interests.

Figures 1-6

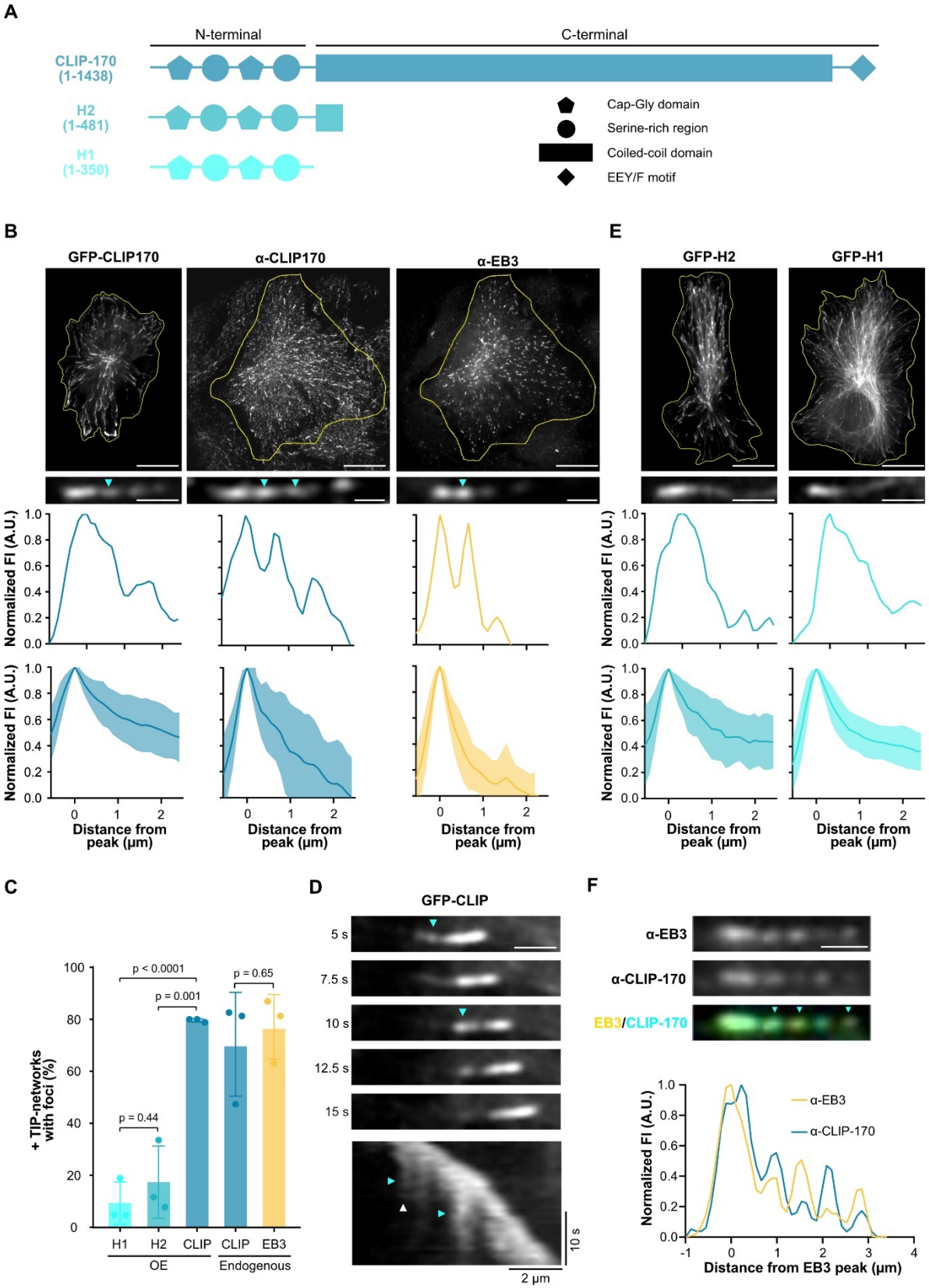
A
N-terminal
C-terminal
CLIP-170 (1-1438)
H2 (1-481)
H1 (1-350)
Cap-Gly domain
Serine-rich region
Coiled-coil domain
EEY/F motif
B
GFP-CLIP170
α-CLIP170
α-EB3
E
GFP-H2
GFP-H1
Normalized FI (A.U.)
Distance from peak (µm)
C
+ TIP-networks with foci (%)
p < 0.0001
p = 0.001
p = 0.65
p = 0.44
H1
H2
CLIP
CLIP
EB3
OE
Endogenous
D
GFP-CLIP
5 s
7.5 s
10 s
12.5 s
15 s
10 s
2 µm
F
α-EB3
α-CLIP-170
EB3/CLIP-170
Normalized FI (A.U.)
Distance from EB3 peak (µm)

506

507 **Figure 1: In cells the EB3/CLIP-170 +TIP-network displays liquid properties at microtubule**
508 **tips.**
509 (**A**) Secondary structure of CLIP-170 (1-1438), H2 (1-481) and H1 (1-350) based on (Pierre et al.,
510 1994; Diamantopolous et al., 1999; Goodson et al., 2003). (**B**) Representative images (top) of fixed
511 RPE-1 cells transfected with full length GFP-CLIP-170 or WT RPE-1 cells stained with antibodies
512 to endogenous CLIP-170 and EB3. Representative profiles of +TIP-networks with matching
513 fluorescence line scans (bottom). Cyan arrowheads indicate tailing foci. Scale bars: 20 µm whole-
514 cell, 2 µm insets. Below are quantified mean line scan profiles (dark line) with standard deviation
515 (shaded area) from 3 independent experiments with a total of: GFP-CLIP-170 57 +TIP-networks
516 from 22 cells; anti-CLIP-170 and anti-EB3 58 +TIP-networks from 12 cells for each condition.
517 (**C**) Percentage of +TIP-networks with foci in fixed cells expressing the indicated CLIP constructs
518 or stained with antibodies to endogenous CLIP-170 or EB3 analysis from B and E. Mean with SD
519 from 3 independent experiments. Statistics: one-way ANOVA test. (**D**) Representative time-lapse
520 images (top) and kymograph (below) of +TIP-network from GFP-CLIP-170 expressing RPE-1
521 cell. Cyan and white arrowheads denote foci formation and dissolving respectively in both time-
522 lapse images and kymograph. Scale bar: 2 µm. (**E**) Representative images of fixed RPE-1 cells
523 transfected with GFP-H2 and GFP-H1. Representative profiles of +TIP-networks with matching
524 fluorescence line scans (bottom). Scale bars: 20 µm whole-cell, 2 µm insets. Below are quantified
525 mean line scan profiles (dark line) with standard deviation (shaded area) from 3 independent
526 experiments with a total of: H2 33 +TIP-networks from 18 cells; H1 47 +TIP-networks from 33
527 cells. (**F**) Representative +TIP-network from cells stained for endogenous EB3 and CLIP-170
528 showing partial co-localization of EB3 and CLIP-170 foci (cyan arrowheads) with corresponding
529 fluorescence line scan below. Scale bar: 1 µm.

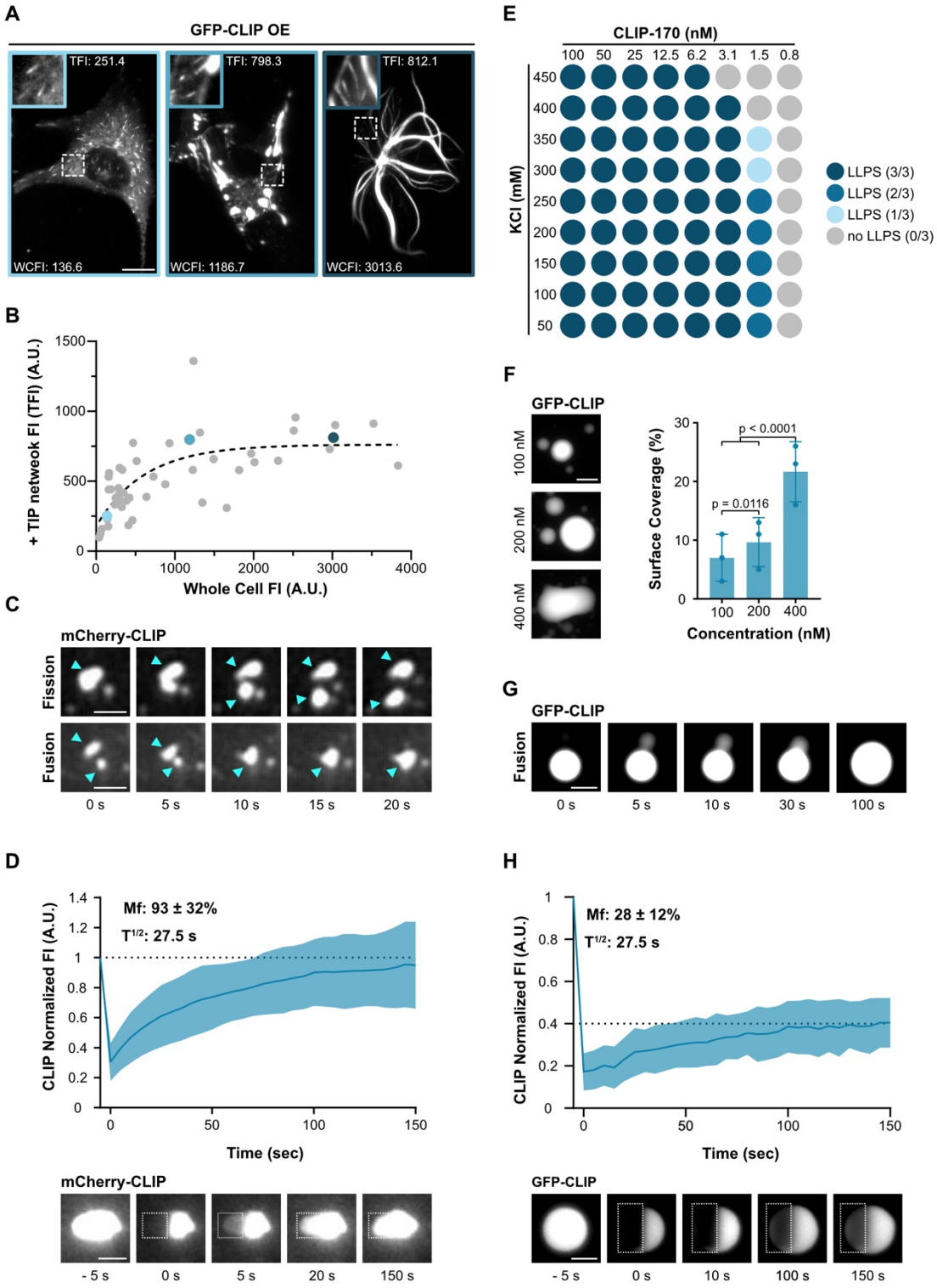
A
GFP-CLIP OE
TFI: 251.4
WCFI: 136.6
TFI: 798.3
WCFI: 1186.7
TFI: 812.1
WCFI: 3013.6
B
+ TIP netweok FI (TFI) (A.U.)
Whole Cell FI (A.U.)
C
mCherry-CLIP
Fission
Fusion
0 s
5 s
10 s
15 s
20 s
D
Mf: 93 ± 32%
T1/2: 27.5 s
CLIP Normalized FI (A.U.)
Time (sec)
mCherry-CLIP
- 5 s
0 s
5 s
20 s
150 s
E
CLIP-170 (nM)
100 50 25 12.5 6.2 3.1 1.5 0.8
KCl (mM)
450 400 350 300 250 200 150 100 50
LLPS (3/3)
LLPS (2/3)
LLPS (1/3)
no LLPS (0/3)
F
GFP-CLIP
100 nM
200 nM
400 nM
Surface Coverage (%)
p < 0.0001
p = 0.0116
Concentration (nM)
G
GFP-CLIP
Fusion
0 s
5 s
10 s
30 s
100 s
H
Mf: 28 ± 12%
T1/2: 27.5 s
CLIP Normalized FI (A.U.)
Time (sec)
GFP-CLIP
- 5 s
0 s
10 s
100 s
150 s

531 **Figure 2: CLIP-170 condenses into droplets in cells and *in vitro*.**
532 (**A**) Representative TIRF images of a RPE-1 cells transfected with GFP-CLIP-170, at three
533 different overexpression levels (see also Figure S2A). Zoom-in shows +TIP-networks with
534 adjusted contrast for visualization. For each cell, the whole cell fluorescence intensity (WCFI) and
535 peak of +TIP network fluorescence intensity (TFI) is indicated, blue outlining of the image
536 corresponds to colored data points in (B). Scale bar: 10 µm. (**B**) Analysis of A showing the
537 correlation between peak +TIP network fluorescence intensity and whole cell fluorescence
538 intensity in RPE-1 cells expressing GFP-CLIP-170. Dashed line shows exponential curve fit. Each
539 dot represents 5 analyzed +TIP-networks from one cell, data from 2 independent experiments with
540 a total of 42 cells. (**C**) Representative TIRF time-lapse images of mCherry-CLIP-170 droplets
541 undergoing fission (top panel, cyan arrowheads), and fusion (bottom panel, cyan arrowheads) in
542 cells. Scale bar: 2 µm. (**D**) Representative TIRF images and recovery curve of mCherry-CLIP-170
543 patches after photobleaching (dashed box). Curve shows mean with SD of 5 individual
544 experiments with a total of 38 droplets from 23 cells. Scale bar: 2 µm. Note that mCherry-CLIP-
545 170 and GFP-CLIP-170 showed the same FRAP-recovery and patch formation behavior (Figures
546 S2A-C) (**E**) Phase diagram of GFP-FL-CLIP *in* vitro at increasing KCl and protein concentration.
547 Blue shaded dot denotes where phase separation occurred, results of 3 independent experiments.
548 (**F**) Representative confocal images of purified GFP-FL-CLIP at indicated concentrations and
549 quantification of the coverslip surface coverage. Statistics: two-tailed Student's *t*-test. Mean with
550 SD from 3 independent experiments with a total of 27 fields of view per condition. Scale bar: 20
551 µm. (**G**) Time-lapse images of purified GFP-FL-CLIP (1 µM) undergoing fusion. Representative
552 of 3 experimental replicates. Scale bar: 10 µm. (**H**) Representative images and recovery curve of
553 purified GFP-FL-CLIP (2 µM) droplets after photobleaching (dashed box). Curve shows mean
554 with SD of 3 individual experiments with a total of 47 condensates. Scale bar: 5 µm.

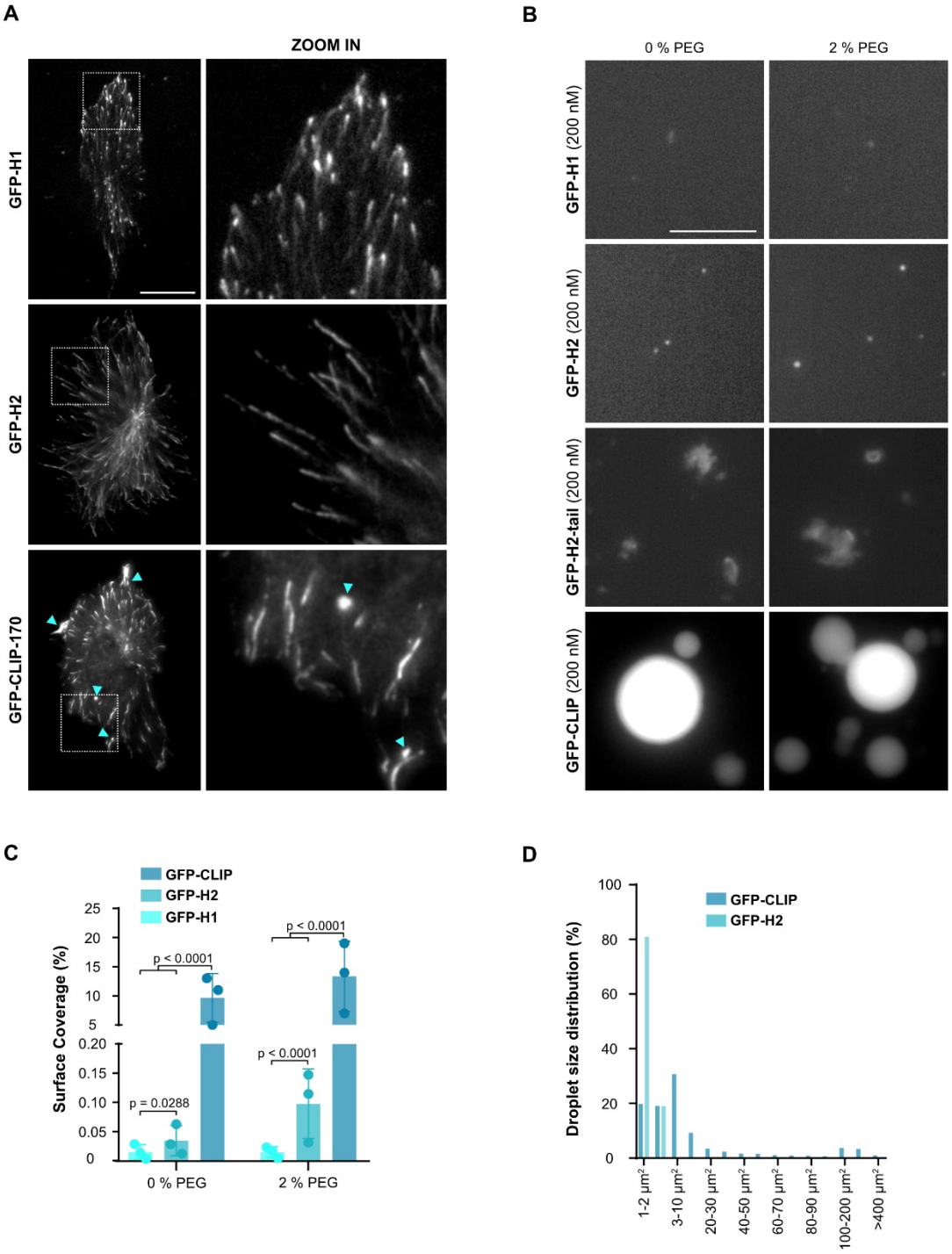
A
ZOOM IN
GFP-H1
GFP-H2
GFP-CLIP-170
B
0 % PEG
2 % PEG
GFP-H1 (200 nM)
GFP-H2 (200 nM)
GFP-H2-tail (200 nM)
GFP-CLIP (200 nM)
C
GFP-CLIP
GFP-H2
GFP-H1
Surface Coverage (%)
p < 0.0001
p < 0.0001
p = 0.0288
p < 0.0001
0 % PEG
2 % PEG
D
GFP-CLIP
GFP-H2
Droplet size distribution (%)
1-2 µm²
3-10 µm²
20-30 µm²
40-50 µm²
60-70 µm²
80-90 µm²
100-200 µm²
>400 µm²

555

556
557 **Figure 3: The C-terminal region drives CLIP-170 into the dense phase.**
558 (**A**) Representative images of fixed RPE-1 cells transfected with full length GFP-CLIP-170, GFP-
559 H2 or GFP-H1 (left panel) with insets (right panel). Cyan arrowheads denote droplet formation in
560 GFP-CLIP-170 expressing cell. Scale bar: 20 µm. (**B**) Representative confocal images of purified
561 GFP-H1, GFP-H2, GFP-H2-tail and GFP-CLIP-170 each at 200 nM in the absence (left panel) or
562 presence (right panel) of 2 % PEG. Scale bar: 20 µm. **(C)** Condensate surface coverage of the three
563 constructs at indicated PEG concentrations. Mean with SD from 3 independent experiments with
564 a total of 27 fields of view per condition. Statistics: two-tailed Student's *t*-test. (**D**) Size distribution
565 of GFP-FL-CLIP (200 nM) and GFP-H2 (200 nM) droplets in the absence of PEG. Graph shows
566 average size distribution from 3 independent experiments with a total of 27 fields of view.
567

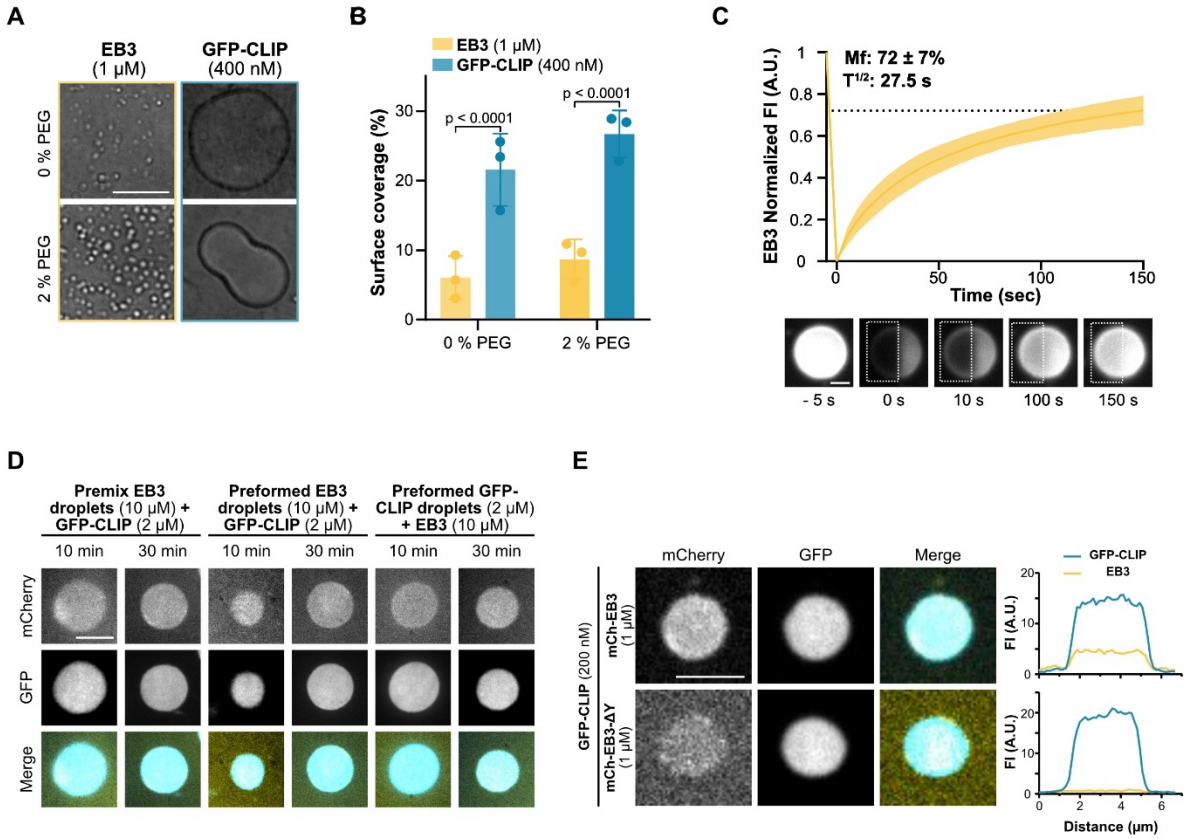

568
569 **Figure 4: EB3 undergoes LLPS and co-condenses with CLIP-170 *in vitro.***
570 (**A**) Representative DIC images of purified EB3 (1 µM) and GFP-FL-CLIP (400 nM) in absence
571 (top panel) or presence (bottom panel) of 2 % PEG. Scale bar: 20 µm. (**B**) Condensate surface
572 coverage of EB3 (1 µM) and GFP-FL-CLIP (400 nM) at indicated PEG concentrations. Mean with
573 SD from 3 independent experiments with a total of 27 fields of view. Statistics: two-tailed
574 Student's *t*-test. (**C**) Representative images and recovery curve of purified EB3 (10 µM) +
575 mCherry-EB3 (100 nM) droplets after photobleaching (dashed box). Curve shows mean with SD
576 of 3 independent experiments with a total of 32 condensates. Scale bar: 5 µm. (**D**) Representative
577 images of 2 µM GFP-FL-CLIP and 10 µM EB3 (8 µM unlabeled + 2 µM mCherry-EB3) in the
578 denoted mixing conditions; 10 min after mixing and at coarsy steady state - 30 min after mixing.

579 Scale bar: 10 μm. (**E**) Representative images of EB3/GFP-FL-CLIP droplets (top) or EB3-
580 ΔY/GFP-FL-CLIP droplets (bottom) at denoted concentrations with the corresponding line scan.
581 Scale bar: 4 μm.
582
583

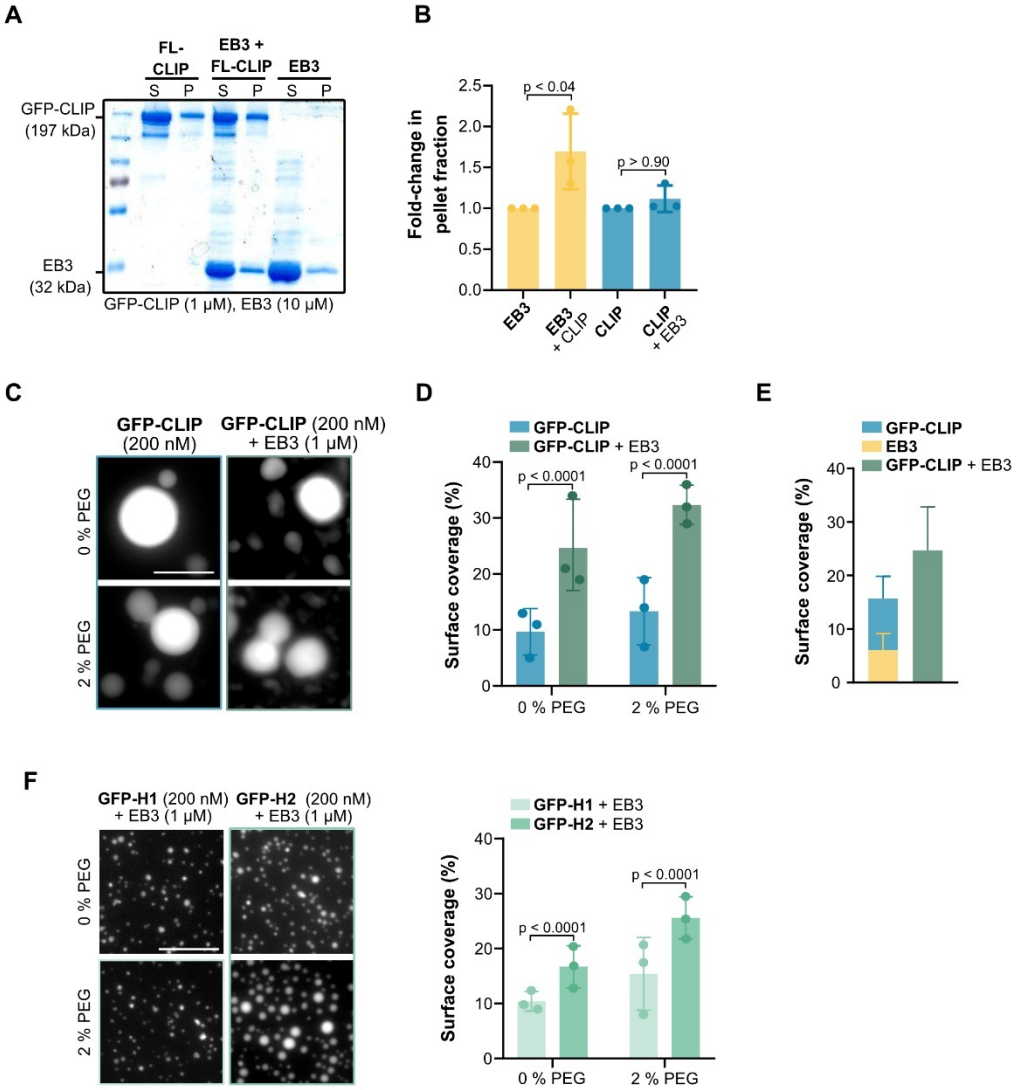
A
FL-CLIP
EB3 + FL-CLIP
EB3
S P S P S P
GFP-CLIP (197 kDa)
EB3 (32 kDa)
GFP-CLIP (1 μM), EB3 (10 μM)
B
Fold-change in pellet fraction
p < 0.04
p > 0.90
EB3
EB3 + CLIP
CLIP
CLIP + EB3
C
GFP-CLIP (200 nM)
GFP-CLIP (200 nM) + EB3 (1 μM)
0 % PEG
2 % PEG
D
GFP-CLIP
GFP-CLIP + EB3
Surface coverage (%)
p < 0.0001
p < 0.0001
0 % PEG
2 % PEG
E
GFP-CLIP
EB3
GFP-CLIP + EB3
Surface coverage (%)
F
GFP-H1 (200 nM) + EB3 (1 μM)
GFP-H2 (200 nM) + EB3 (1 μM)
0 % PEG
2 % PEG
GFP-H1 + EB3
GFP-H2 + EB3
Surface coverage (%)
p < 0.0001
p < 0.0001
0 % PEG
2 % PEG

585 **Figure 5: Synergistic condensation of CLIP-170 and EB3.**
586 (**A**) Representative SDS-PAGE analysis from the droplet-pelleting assay showing protein fractions
587 in supernatant dilute phase (S) or pellet dense phase (P) under each condition: 1 μM GFP-FL-
588 CLIP; 10 μM EB3; EB3/GFP-FL-CLIP (10 μM + 1 μM). (**B**) Quantification of SDS-PAGE
589 analysis showing the fold-change of protein in the pellet fraction at the three conditions. Mean
590 with SD from three independent experiments. Statistics: one-way ANOVA. (**C**) Representative
591 fluorescence confocal images of purified GFP-FL-CLIP in the absence (left) or presence (right) of
592 EB3, and in the absence (top panel) or presence (bottom panel) of 2 % PEG. Scale bar: 20 μm. (**D**)
593 Condensate surface coverage of purified GFP-FL-CLIP in the absence (left) or presence (right) of
594 EB3 at indicated PEG concentrations. Mean with SD from 3 independent experiments with a total
595 of 27 fields of view. Statistics: two-tailed Student's *t*-test. (**E**) Quantification of droplet surface
596 coverage of EB3 and GFP-FL-CLIP alone compared to surface coverage of EB3/GFP-FL-CLIP
597 droplet formation when undergoing synergistic LLPS in the absence of PEG. (**F**) Representative
598 fluorescence confocal images and quantification of purified GFP-H1 (left) or GFP-H2 (right) in
599 the presence of EB3, and in the absence (top panel) or presence (bottom panel) of 2 % PEG. Scale
600 bar: 20 μm. Right: condensate surface coverage of indicated GFP-H1 (200 nM) or GFP-H2 (200
601 nM) in the presence of EB3 (1 μM), and in the presence of the indicated PEG concentrations. Mean
602 with SD from 3 independent experiments with a total of 27 fields of view. Statistics: two-tailed
603 Student's *t*-test.
604
605
606
607

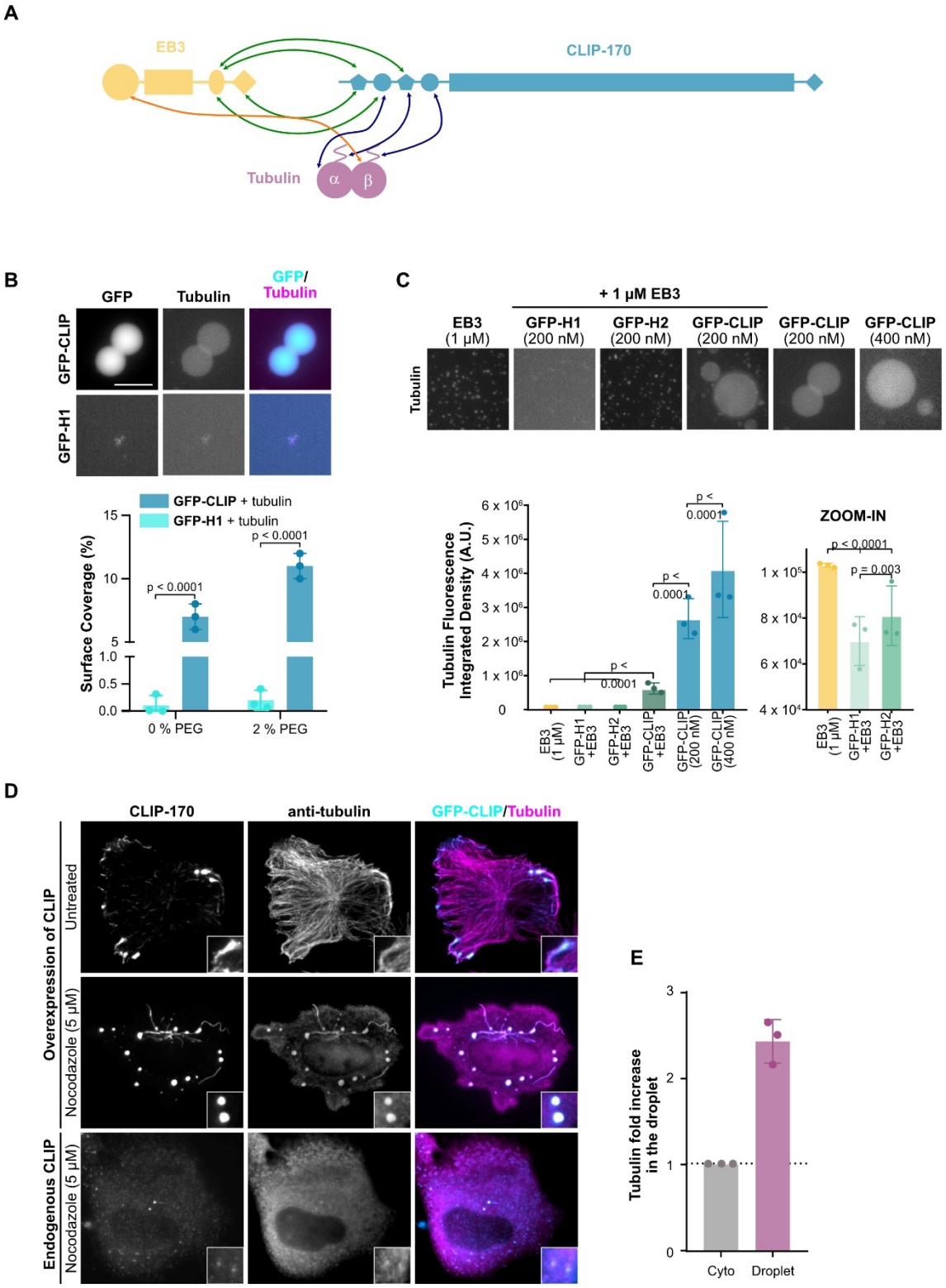
A
EB3
CLIP-170
Tubulin
α
β
B
GFP
Tubulin
GFP/
Tubulin
GFP-CLIP
GFP-H1
GFP-CLIP + tubulin
GFP-H1 + tubulin
Surface Coverage (%)
p < 0.0001
p < 0.0001
0 % PEG
2 % PEG
C
+ 1 μM EB3
EB3
(1 μM)
GFP-H1
(200 nM)
GFP-H2
(200 nM)
GFP-CLIP
(200 nM)
GFP-CLIP
(200 nM)
GFP-CLIP
(400 nM)
Tubulin
Tubulin Fluorescence
Integrated Density (A.U.)
ZOOM-IN
p < 0.0001
p = 0.003
EB3
(1 μM)
GFP-H1
+EB3
GFP-H2
+EB3
GFP-CLIP
+EB3
GFP-CLIP
(200 nM)
GFP-CLIP
(400 nM)
D
CLIP-170
anti-tubulin
GFP-CLIP/Tubulin
Overexpression of CLIP
Untreated
Nocodazole (5 μM)
Endogenous CLIP
Nocodazole (5 μM)
E
Tubulin fold increase
in the droplet
Cyto
Droplet

Figure 6: CLIP-170 and EB3 droplets condense tubulin.
(**A**) Cartoon schematic of domain interactions between EB3, CLIP-170, and tubulin based primarily on (Gupta et al., 2010; Chen et al., 2021; Bjelic et al., 2012). Interaction sites between EB3 and CLIP-170, EB3 and tubulin, and CLIP-170 and tubulin are shown with green, orange, and blue arrows, respectively. For simplification, monomers of EB3 and CLIP-170 are shown. (**B**) Top: representative confocal images of purified GFP-FL-CLIP and GFP-H1 each at 200 nM with Atto-565-tubulin (400 nM). Scale bar: 20 µm. Bottom: quantification of the coverslip surface coverage of tubulin in presence of GFP-FL-CLIP or GFP-H1. Mean with SD from 3 independent experiments with a total of 27 fields of view. Statistics: two-tailed Student's *t*-test. Note that co-condensation is independent of the fluorescent tag, as unlabeled tubulin also partitioned into GFP-FL-CLIP droplets see Figure S6B. (**C**) Top: representative confocal images of Atto-565-tubulin (400 nM) in the presence of purified EB3 (1 µM), GFP-H1 (200 nM) and EB3 (1 µM), GFP-H2 (200 nM) and EB3 (1 µM), GFP-FL-CLIP (200 nM) and EB3 (1 µM), and GFP-FL-CLIP (200 nM and 400 nM) alone. Scale bar: 20 µm. Bottom: quantification of the integrated density of tubulin fluorescence under denoted conditions with zoom in for the first three conditions. Mean with SD from 3 independent experiments with a total of 27 fields of view. Statistics: two-tailed Student's *t*-test. (**B-C**) Note that droplet centrifugation onto the coverslip lead to a homogenous distribution of tubulin in the GFP-FL-CLIP droplet, see Figure S6B (**D**) Representative images of fixed RPE-1 cells transfected with GFP-CLIP-170 and untreated (top panel) or treated with 5 µM nocodazole for 1 hour (middle panel); RPE-1 WT cells were treated with 5 µM nocodazole (bottom panel) and stained for endogenous CLIP-170 and tubulin. Scale bar: 10 µm. Images are representative of 3 independent experiments. **(E)** Graph showing normalized tubulin fluorescence intensity in CLIP-170 droplets compared to cytoplasm in full-length GFP-CLIP-170 transfected RPE-1 cells treated with nocodazole. Mean with SD from 3 independent experiments with a total of 126 condensates from 26 cells.

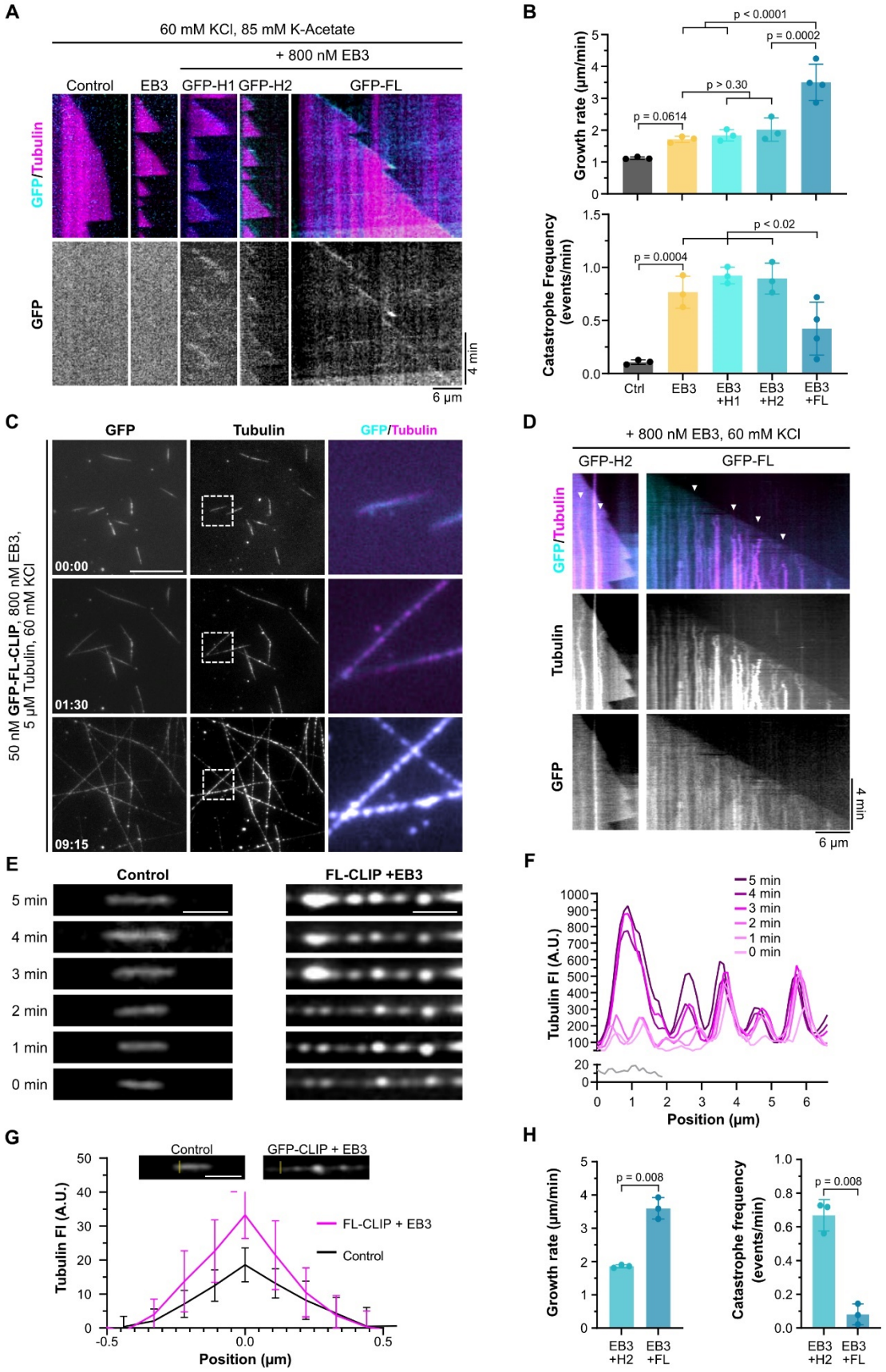
A
60 mM KCl, 85 mM K-Acetate
+ 800 nM EB3
Control
EB3
GFP-H1
GFP-H2
GFP-FL
GFP/Tubulin
GFP
4 min
6 µm
B
Growth rate (µm/min)
p < 0.0001
p = 0.0002
p > 0.30
p = 0.0614
Catastrophe Frequency (events/min)
p < 0.02
p = 0.0004
Ctrl
EB3
EB3 +H1
EB3 +H2
EB3 +FL
C
GFP
Tubulin
GFP/Tubulin
50 nM GFP-FL-CLIP, 800 nM EB3, 5 µM Tubulin, 60 mM KCl
00:00
01:30
09:15
D
+ 800 nM EB3, 60 mM KCl
GFP-H2
GFP-FL
GFP/Tubulin
Tubulin
GFP
4 min
6 µm
E
Control
FL-CLIP +EB3
5 min
4 min
3 min
2 min
1 min
0 min
F
5 min
4 min
3 min
2 min
1 min
0 min
Tubulin FI (A.U.)
Position (µm)
G
Control
GFP-CLIP + EB3
FL-CLIP + EB3
Control
Tubulin FI (A.U.)
Position (µm)
H
Growth rate (µm/min)
p = 0.008
EB3 +H2
EB3 +FL
Catastrophe frequency (events/min)
p = 0.008
EB3 +H2
EB3 +FL

636

637 **Figure 7: LLPS of +TIPs regulates microtubule dynamics through local tubulin**
638 **condensation.**
639 **(A)** Representative microtubule kymographs of denoted +TIP-networks in higher salt buffer (60
640 mM KCl and 85 mM K-acetate, see materials and methods). Note that tip-tracking efficiency (GFP
641 channel) is weaker at 5 µM tubulin than at higher tubulin concentrations (Figure S8B). (**B**)
642 Microtubule growth rate (top) and catastrophe frequency (bottom) in presence of denoted proteins
643 in high salt buffer. Mean with SD of minimum of three independent experiments with the following
644 number of analyzed microtubules: Control – 48; EB3 – 31; EB3/H1 – 28; EB3/H2 – 28; EB3/FL-
645 CLIP - 60. Statistics: One-way ANOVA Fisher's LSD test. (**C**) Representative time-lapse TIRF
646 images of GFP-FL-CLIP (50 nM) with Atto-565-tubulin (5 µM) in the presence of unlabeled EB3
647 (800 nM) and 60 mM KCl. Time denoted in minutes: seconds; scale bar: 20 µm. The zoom-ins
648 (white dashed box) show representative droplet formation along microtubules. (**D**) Representative
649 microtubule kymographs in the presence of GFP-H2 or GFP-FL-CLIP (50 nM) and EB3 (800 nM)
650 grown at 5 µM tubulin and 60 mM KCl. Arrowheads denote areas of robust tubulin/FL-CLIP
651 condensation on growing microtubule shaft. (**E**) Representative images of Atto-565-tubulin
652 microtubules growing in the absence (left, control) and in presence of EB3/FL-CLIP (right). Right
653 images show tubulin condensation along microtubule over time. Scale bar: 2 µm. (**F**)
654 Corresponding line scan of E with the gray line scan representing the 5 µM tubulin control
655 condition and the magenta line scans of 5 µM tubulin in presence of EB3/FL-CLIP (800 nM/50
656 nM). (**G**) Tubulin fluorescence intensity in tip-proximal regions in 5 µM tubulin control condition
657 and in presence of EB3/FL-CLIP. Quantification of perpendicular line scans in tip-proximal
658 regions. Mean with SD from 2 independent experiments for each condition and a total of 20
659 microtubules; Scale bar: 2 µm. (**H**) Quantification of microtubule growth rate (left) and catastrophe
660 frequency (right) in the presence of EB3/H2-networks and EB3/FL-CLIP droplets in experiments
661 from D (60 mM KCl). Mean with SD of three independent experiments with the following number
662 of analyzed microtubules: EB3/H2 – 29; EB3/FL-CLIP – 59. Statistics: paired t-test.

663

664

	C_{dilute} (nM)	$C_{droplet}$ (nM)	Ratio ($C_{droplet}/C_{dilute}$)
CLIP-170 (200 nM)	70	1 700	24
mcherry-EB3 (2 µM) + EB3 (8 µM)	8 600	31 000	3.5
CLIP-170 (200 nM) + mcherry-EB3 (1 µM)	75	1 800	24
mcherry-EB3 (1 µM) + CLIP-170 (200 nM)	400	2 000	5
CLIP-170 (200 nM) + tubulin (400 nM)	50	1 700	34
Tubulin (400 nM) + CLIP-170 (200 nM)	300	Droplet 650 / Shell 1 200	Droplet 2 / Shell 4

665
666 **Table 1: CLIP-170 , EB3 and tubulin concentration inside droplets.**
667 Protein concentration outside droplets (C_{dilute}) and inside droplets ($C_{droplet}$), obtained by calibrating
668 fluorescent intensities of GFP, mCherry and Atto-565 see calibration in Figure S9.

669

Supplementary Figures S1-S6

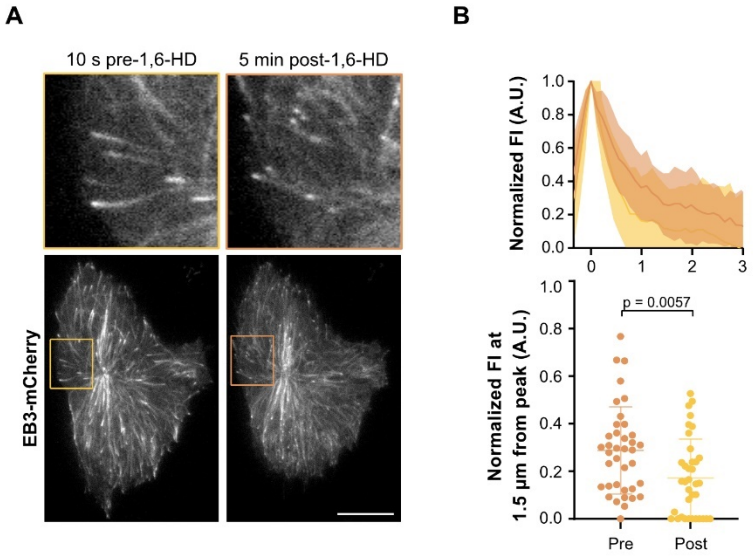

Figure S1: Decrease in EB3 network size upon treatment with 1,6-HD.
(A) Representative images of CRISPR/Cas9 knock-in RPE-1-GFP-Tubulin cells expressing EB3-mCherry before and after 5-minute treatment with 5 % 1,6-hexanediol, with insets. Scale bar: 20 µm. **(B)** Top: mean fluorescence intensity profile of +TIP-networks before and after 1,6-hexanediol treatment. Bottom: normalized fluorescence intensity of +TIP-networks 1.5 µm away from the peak. Mean with SD of 36-38 +TIP-networks from 6 cells from 2 independent experiments. Statistics: paired t-test. Note that CLIP-170 patches were not dissolved by 1,6-hexanediol treatment.

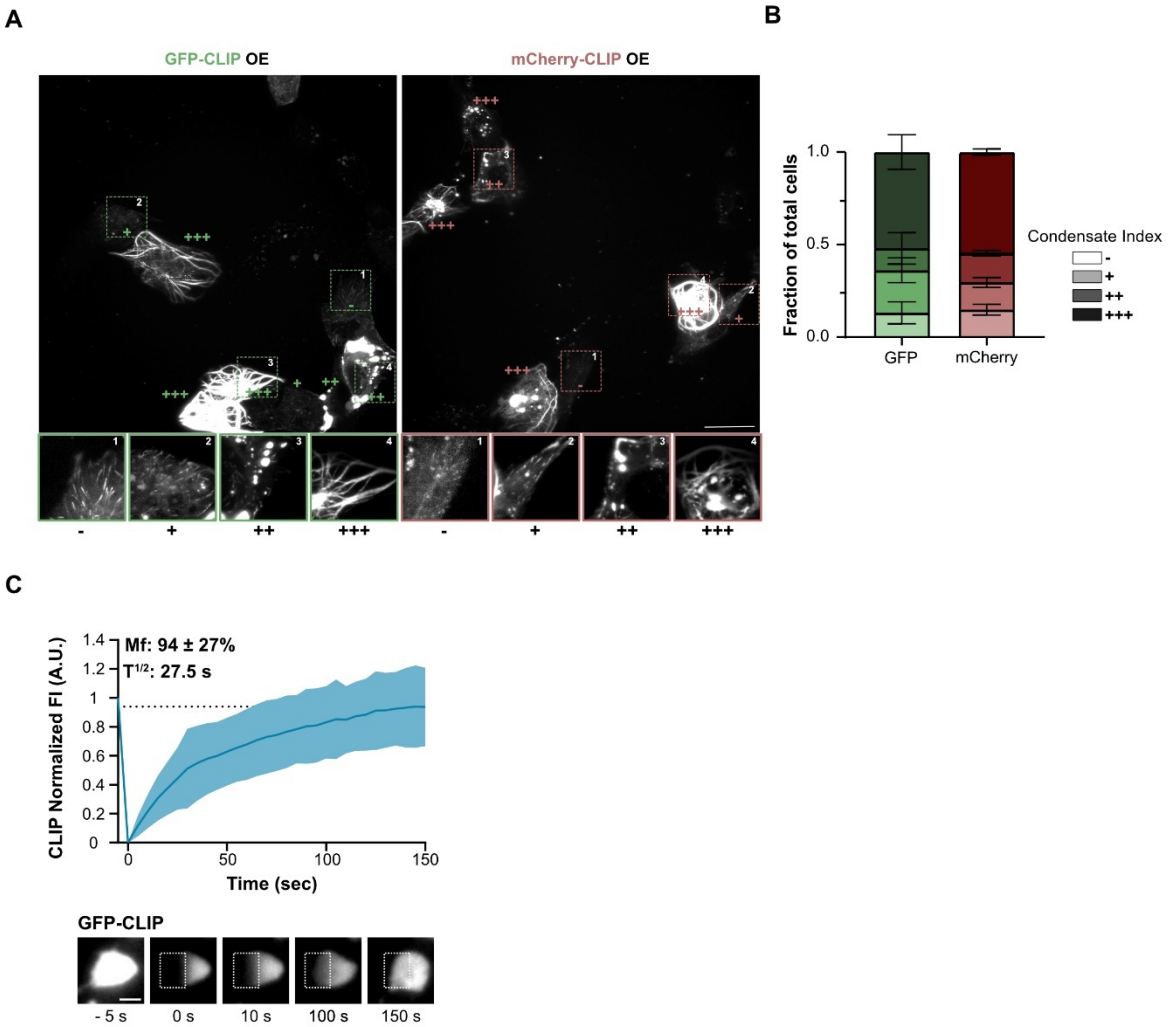

Figure S2: Fluorescent tag do not impact on LLPS of CLIP-170 in cells.
(A) Representative images (top) with zoom-in (bottom) of RPE-1 cells expressing GFP- (left) or mCherry-CLIP (right) with indicated index for different condensation phenotypes. -: no observed cytoplasmic condensates; +: few small cytoplasmic condensates; ++: several large or many small condensates; +++: many large condensates and/or coating/bundling of microtubules. Note that zoom-in are contrast-adjusted. Scale bar: 30 µm. **(B)** Quantification of condensation index from experiments shown in A. Mean with SD from 2 independent experiments with 100 cells per experiment. (**C**) Representative TIRF images (bottom) and recovery curve (top) of GFP-CLIP-170 droplets in RPE-1 cells after photobleaching (dashed box). Mean with SD of 3 individual experiments with a total of 36 droplets from 24 cells. Scale bar: 2 µm.

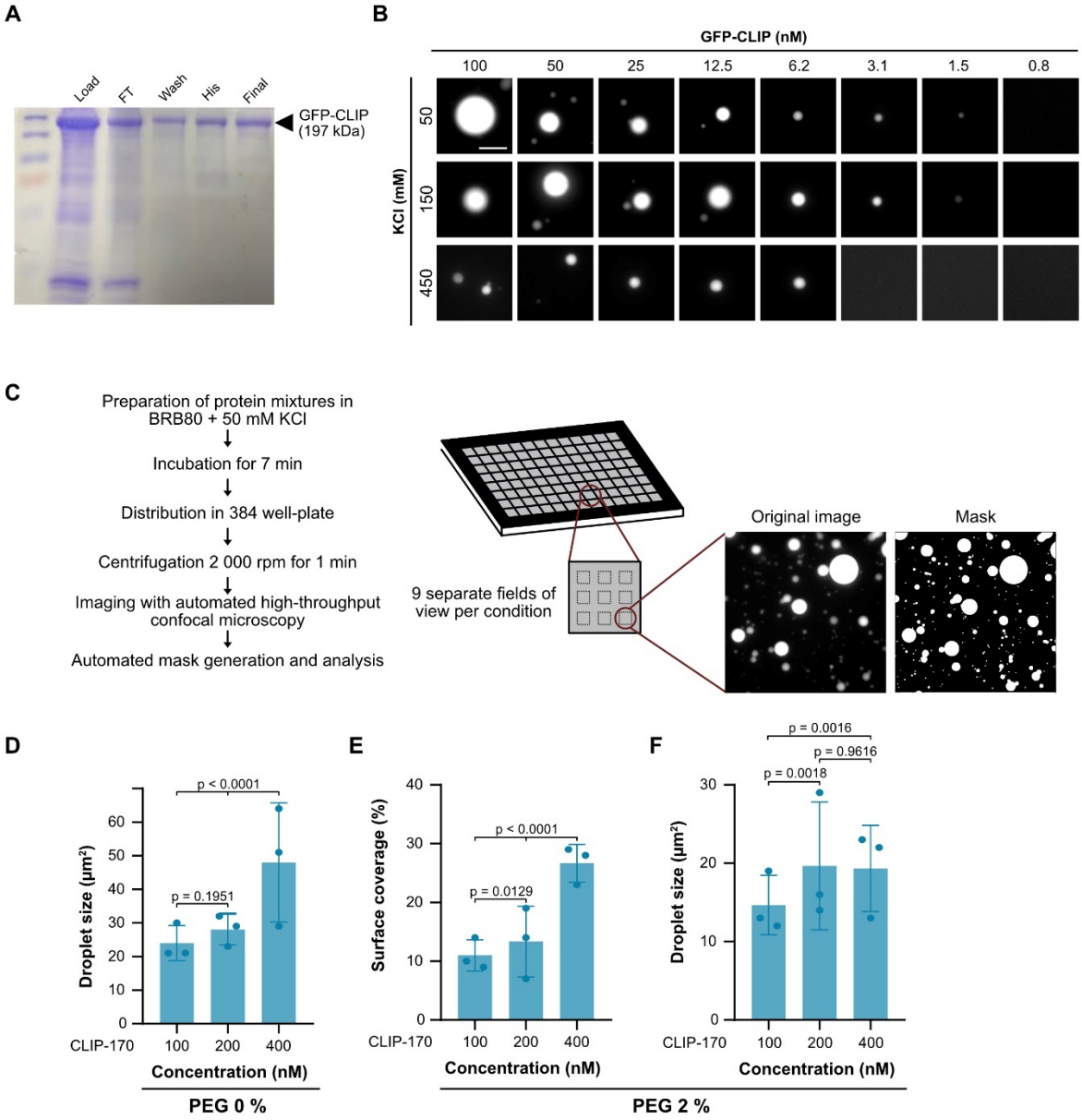

Figure S3: CLIP-170 droplet formation *in vitro* depends on molecular crowding, protein and salt concentrations.

(**A**) SDS-PAGE analysis of GFP-FL-CLIP protein purification. Load, lysate loaded onto HisTRAP column; FT, flow through; wash, fractions collected during HisTRAP-column washing; final, final concentrated protein sample post-SEC and post-concentration. (**B**) Representative images of GFP-FL-CLIP phase diagram for 50, 150 and 450 mM KCl at indicated protein concentrations from 3 independent experiments. Scale bar: 10 µm. (**C**) Experimental outline for high throughput phase separation assays. For details, see materials and methods. (**D**) Droplet size (area) for GFP-FL-CLIP condensates at 100, 200, or 400 nM in the absence of PEG. (**E**) Coverslip surface coverage of GFP-FL-CLIP at the indicated concentrations in the presence of 2% PEG. (**F**) Droplet size (area) of GFP-FL-CLIP condensates at 100, 200 and 400 nM in the presence of 2 % PEG. Mean with SD

716 from 3 independent experiments with a total of 27 fields of view. Statistics: two-tailed Student's *t*-
717 test.

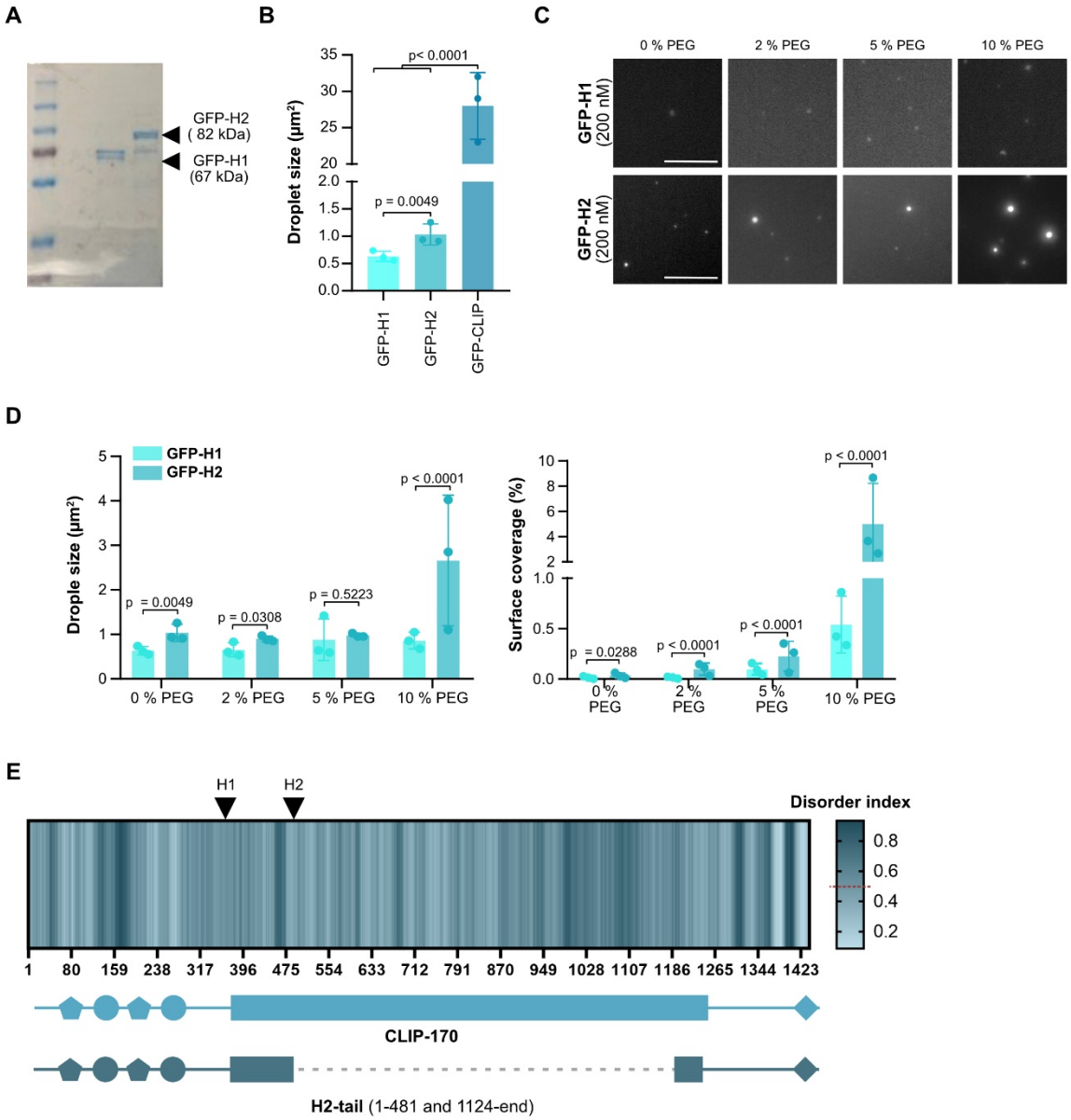

718
719 **Figure S4: H2 only weakly undergoes LLPS even under strong molecular crowding**
720 **conditions.**
721 (**A**) SDS-PAGE analysis of purified GFP-H1 and GFP-H2 protein. (**B**) Droplet size (area) of GFP-
722 H2 (200 nM) and GFP-FL-CLIP (200 nM), and aggregate size of GFP-H1 (200 nM) in the absence
723 of PEG. Mean with SD from 3 independent experiments with a total of 27 fields of view. Statistics:
724 one-way ANOVA test. (**C**) Representative fluorescence confocal images of A in the presence of
725 0, 2, 5 and 10 % PEG. Scale bar: 20 µm. (**D**) Droplet size (left graph) and surface coverage (right
726 graph) of denoted proteins at indicated PEG concentrations. Mean with SD of from 27 fields of
727 view from 3 independent experiments. Statistics: two-tailed Student's *t*-test.

(E) Top: prediction of intrinsic disorder regions in CLIP-170, based on IUPred2A software. Values above the red dotted line (0.5) are considered as disordered (Mészáros et al., 2018). Dark blue corresponds to highly disordered regions. Bottom: CLIP-170 and mutant H2-tail secondary structures, length of H1 and H2 is indicated, black arrowhead.

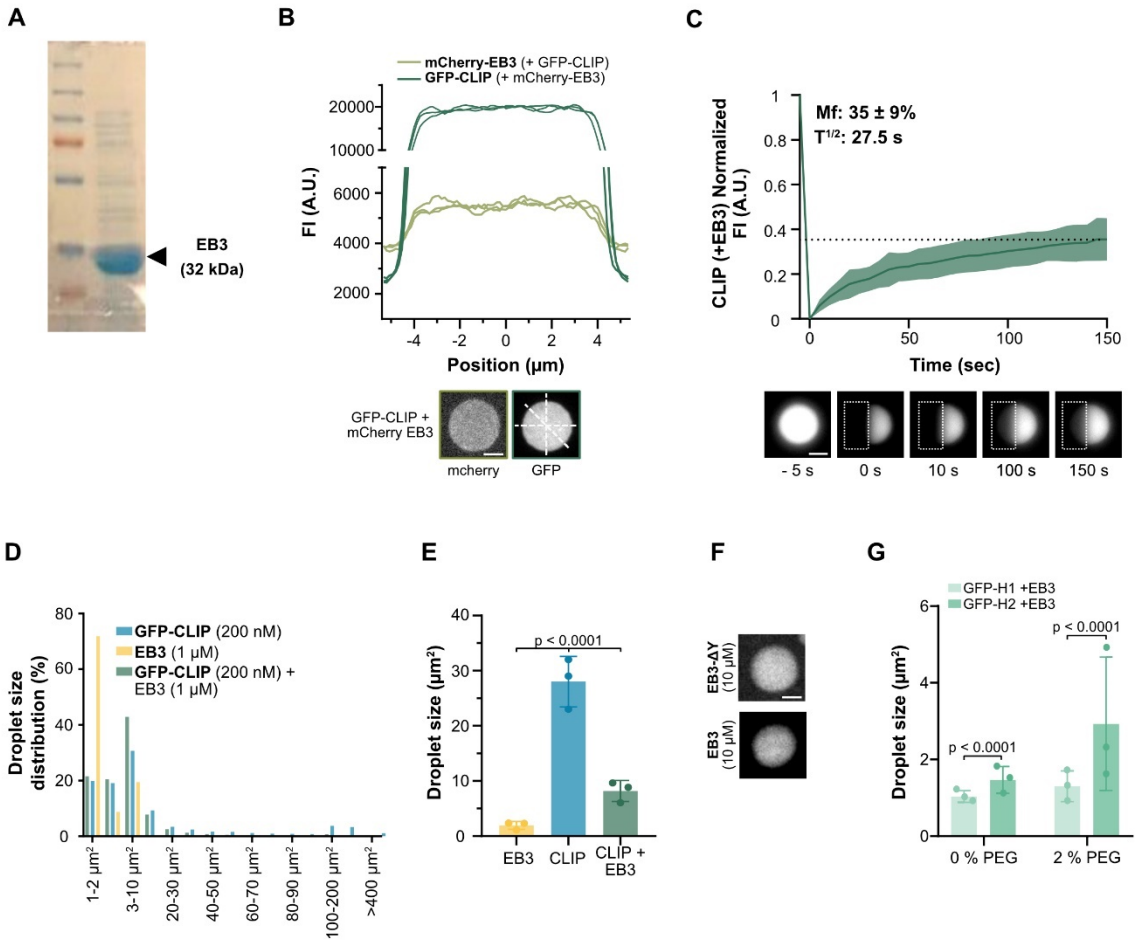

Figure S5: EB3/CLIP-170 phase separation is driven by the CLIP-170 C-terminal region *in vitro.* (**A**) SDS-PAGE analysis of purified EB3. (**B**) Line scan (top) with corresponding images (bottom, white lines indicate the line scans) of EB3/FL-CLIP droplets showing a homogenous protein distribution. GFP-FL-CLIP (2 µM) EB3 (8 µM unlabeled EB3 + 2 µM mCherry-EB3). (**C**) Representative images and recovery curve of purified EB3/GFP-FL-CLIP (10 µM / 2 µM) droplets after photobleaching (dashed box). Mean with SD of 3 independent experiments with a total of 35 condensates. Scale bar: 5 µm. (**D**) Size distribution of GFP-FL-CLIP (200 nM), EB3 (1 µM) and the EB3/FL-CLIP droplets in the absence of PEG. Mean size distribution from 3 independent experiments with a total of 27 fields of view. (**E**) Droplet size (area) of unlabeled EB3 (1 µM), GFP-FL-CLIP (200 nM) and EB3/FL-CLIP (1 µM + 200 nM) in absence of PEG. Mean with SD of 3 independent experiments with a total of 27 fields of view. Statistics: two-tailed Student's *t*-test. (**F**) Representative images of EB3-ΔY condensates (8 µM unlabeled and 2 µM mCherry-EB3-ΔY) and EB3 (8 µM unlabeled and 2 µM mCherry-EB3). Scale bar: 4 µm. (**G**) Condensate

747 size (area) of GFP-H1 (200 nM) or GFP-H2 (200 nM) in the presence of EB3 (1 μM) in the absence
748 or presence of 2% PEG. Mean with SD of 3 independent experiments with a total of 27 fields of
749 view. Statistics: two-tailed Student's *t*-test.
750
751

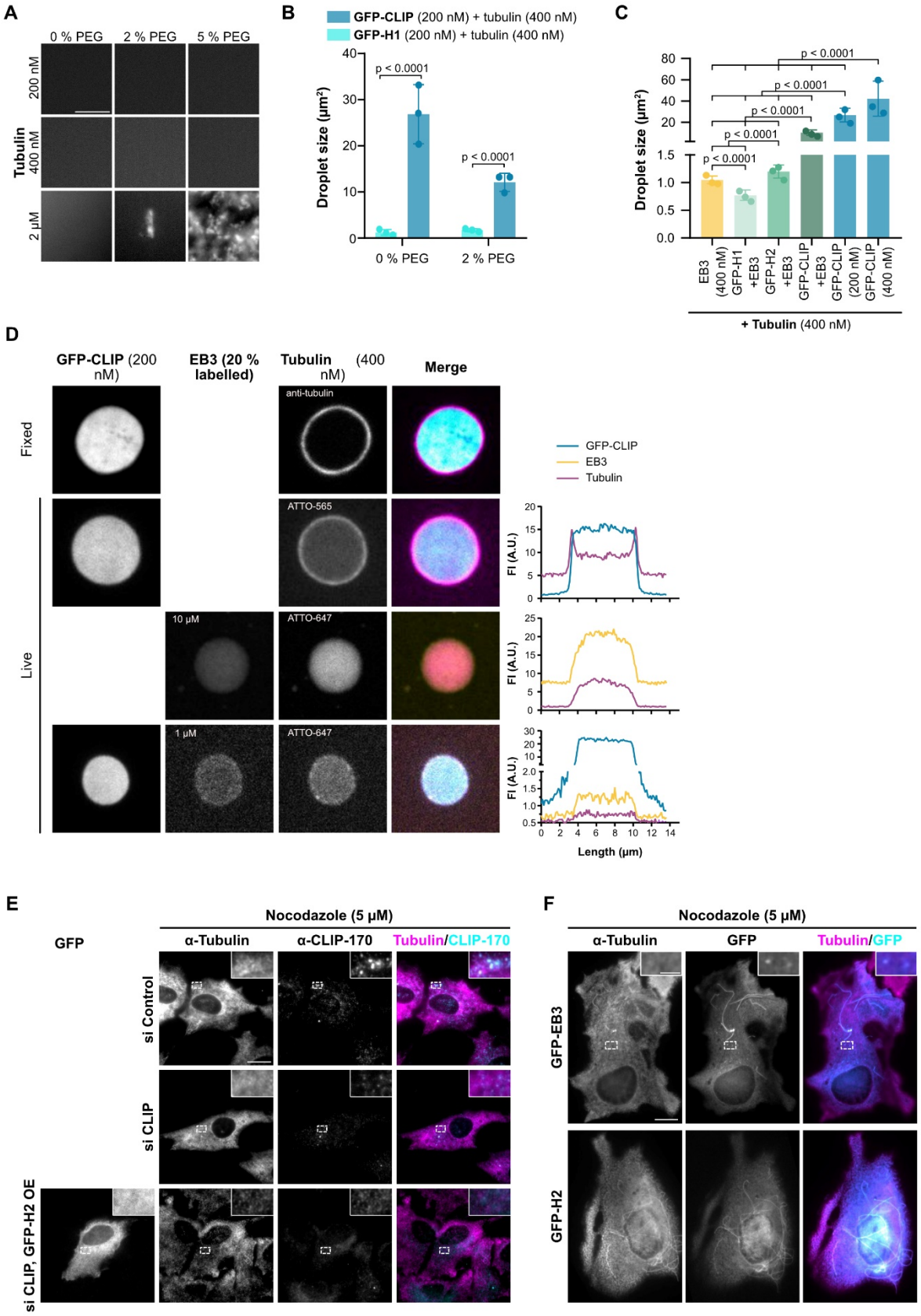
A
0 % PEG
2 % PEG
5 % PEG
Tubulin
200 nM
400 nM
2 µM
B
GFP-CLIP (200 nM) + tubulin (400 nM)
GFP-H1 (200 nM) + tubulin (400 nM)
Droplet size (µm²)
p < 0.0001
0 % PEG
2 % PEG
C
Droplet size (µm²)
EB3 (400 nM)
GFP-H1
+EB3
GFP-H2
+EB3
GFP-CLIP
+EB3
GFP-CLIP (200 nM)
GFP-CLIP (400 nM)
+ Tubulin (400 nM)
D
GFP-CLIP (200 nM)
EB3 (20 % labelled)
Tubulin (400 nM)
Merge
Fixed
Live
anti-tubulin
ATTO-565
10 µM
ATTO-647
1 µM
ATTO-647
GFP-CLIP
EB3
Tubulin
FI (A.U.)
Length (µm)
E
Nocodazole (5 µM)
GFP
α-Tubulin
α-CLIP-170
Tubulin/CLIP-170
si Control
si CLIP
si CLIP, GFP-H2 OE
F
Nocodazole (5 µM)
α-Tubulin
GFP
Tubulin/GFP
GFP-EB3
GFP-H2

752

753 **Figure S6: CLIP-170 and EB3 form a tubulin-condensing network.**
754 **(A)** Representative fluorescence confocal images of purified Atto-565-tubulin at indicated
755 concentrations in presence of 0, 2 and 5 % PEG. Note that at 2 μM tubulin, PEG caused
756 aggregation (but not condensate formation) of tubulin. Scale bar: 20 μm. (**B**) Quantified droplet
757 size of Atto-565-tubulin (400 nM) in the presence of GFP-H1 (200 nM) or GFP-FL-CLIP (200
758 nM) in the absence or presence of 2% PEG. Mean with SD of from 27 fields of view from 3
759 independent experiments. Statistics: two-tailed Student's *t*-test (right graph). (**C**) Quantified
760 droplet size (area) of Atto-565-tubulin (400 nM) in the presence of purified EB3 (1 μM), GFP-H1
761 (200 nM) and EB3 (1 μM), GFP-H2 (200 nM) and EB3 (1 μM), GFP-FL-CLIP (200 nM) and EB3
762 (1 μM), GFP-FL-CLIP (200nM) alone, and GFP-FL-CLIP (400nM) alone. Mean with SD of three
763 independent experiments. Statistic: two-tailed Student's *t*-test. (**D**) Representative images of
764 tubulin/FL-CLIP droplets (unlabeled tubulin) fixed and immunostained using tubulin specific
765 antibodies (top). Representative images of GFP-FL-CLIP (200 nM) + tubulin-565 (400 nM)
766 droplets, EB3 (8 μM) + mCherry-EB3 (2 μM) + tubulin-647 (4 μM) droplets and EB3 (900 nM)
767 + mCherry-EB3 (100 nM) + GFP-FL-CLIP (200 nM) + tubulin-647 (400 nM) droplets with the
768 corresponding line scans. Scale bar: 5 μm. (**E**) Representative images of fixed RPE-1 cells
769 transfected with control siRNA (top panel), CLIP-170 siRNA (middle panel), or CLIP-170 siRNA
770 rescued with GFP-H2 (bottom panel) treated with 5 μM nocodazole for 1 hour and stained for
771 tubulin. Zoom-in of regions indicated by dashed box. Scale bar: 10 μm. (**F**) Representative images
772 of fixed RPE-1 cells transfected with GFP-H2 (top panel) or GFP-EB3 (bottom panel) treated with
773 5 μM nocodazole for 1 hour and stained for tubulin. Zoom-in of regions indicated by dashed box
774 Scale bar: 10 μm.
775

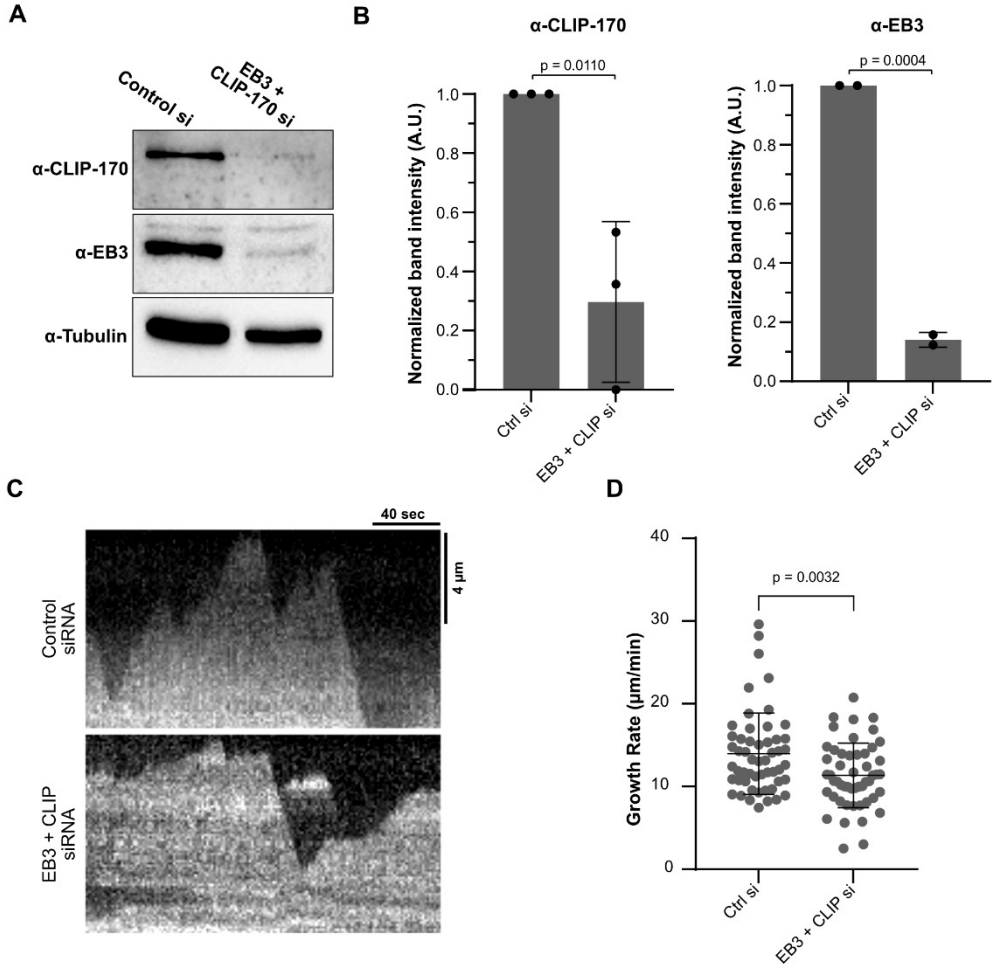

Figure S7: Depletion of EB3/CLIP-170 networks reduce microtubule growth rates in RPE-1 cells.

(**A**) Representative Western Blot of CRISPR/Cas9 knock-in GFP-Tubulin RPE-1 cells transfected with control siRNA or siRNA to CLIP-170 and EB3 simultaneously for 72 hours. (**B**) Quantification of western blot of CLIP-170 depletion (left) and EB3 depletion (right) in cells treated with either control or EB3 + CLIP-170 siRNAs. Graphs show mean with SD from 3 (α-CLIP-170) or 2 (α-EB3) individual experiments. Statistics: paired t-test.(**C**) Representative microtubule kymographs from CRISPR/Cas9 knock-in RPE-1-GFP-Tubulin cells transfected with either control (top) or EB3 + CLIP-170 (bottom) siRNAs for 72 hours. (**D**) Mean microtubule growth rate with SD from: Control – 53 microtubules from 29 cells; EB3 + CLIP siRNA – 51 microtubules from 19 cells (4 independent experiments per condition). In graph, each dot represents a single microtubule. Statistics: paired t-test.

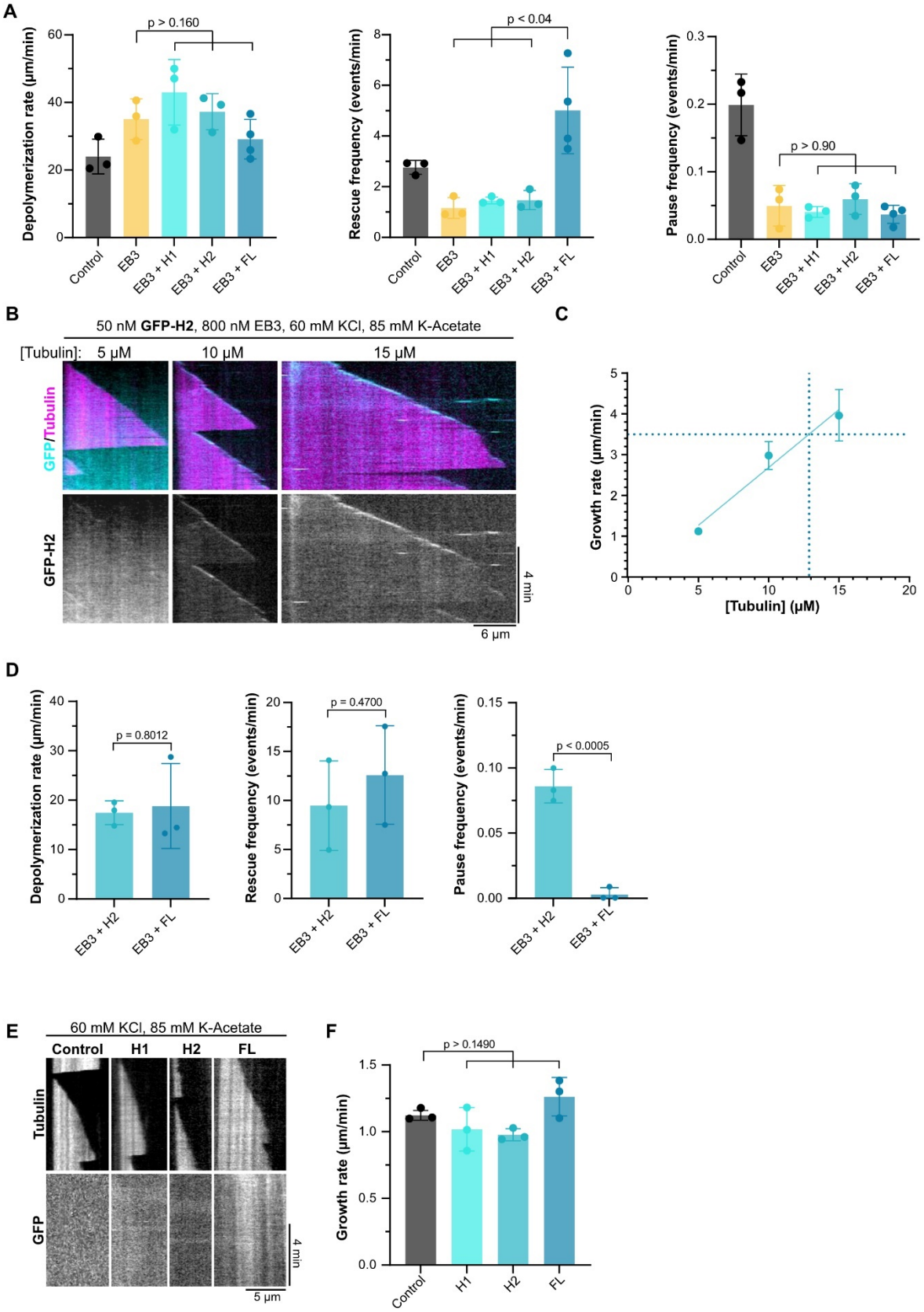
A
Depolymerization rate (µm/min)
p > 0.160
Rescue frequency (events/min)
p < 0.04
Pause frequency (events/min)
p > 0.90
Control
EB3
EB3 + H1
EB3 + H2
EB3 + FL
B
50 nM GFP-H2, 800 nM EB3, 60 mM KCl, 85 mM K-Acetate
[Tubulin]: 5 µM
10 µM
15 µM
GFP/Tubulin
GFP-H2
4 min
6 µm
C
Growth rate (µm/min)
[Tubulin] (µM)
D
p = 0.8012
p = 0.4700
p < 0.0005
EB3 + H2
EB3 + FL
E
60 mM KCl, 85 mM K-Acetate
Control
H1
H2
FL
Tubulin
GFP
4 min
5 µm
F
p > 0.1490

790

Figure S8: Phase separation potent +TIP-networks impart stronger effects on microtubule dynamics

(**A**) Microtubule dynamic parameters (depolymerization rate, left; rescue frequency, middle; and pause frequency, right) for the denoted conditions in 60 mM KCl and 85 mM K-acetate (corresponding assay to Figure 6B, see here for number of analyzed microtubules). Mean with SD of three individual experiments. Statistics: one-way ANOVA Fisher's LSD test (**B**) Representative microtubule kymographs in the presence of GFP-H2 (50 nM) and EB3 (800 nM) grown at the denoted tubulin and salt concentrations. (**C**) Microtubule growth rate from experiments in B. Mean with SD from three individual experiments. Solid cyan line shows linear regression curve fit. Dashed blue line indicates concentration of tubulin at which microtubule in presence of EB3/H2 networks grow at 3.8 µm/min (the speed achieved by EB3/FL-CLIP droplets at 5 µM tubulin; Figure 6A). (**D**) Microtubule dynamic parameters (depolymerization rate, left; rescue frequency, middle; and pause frequency, right) for the denoted conditions in 60 mM KCl (corresponding assay to Figure 6H, see here for number of analyzed microtubules). Mean with SD from minimum three independent experimental replicates. Statistics: one-way ANOVA Fisher's LSD test (**E**) Representative microtubule kymographs of control (only tubulin), 50 nM GFP-H1, 50 nM GFP-H2 or 50 nM FL-CLIP. (**F**) Microtubule growth rate from experiments in Figure E. Mean with SD from three independent experiments. Total number of MTs analyzed per condition: Control – 48; H1 – 42; H2 – 41; FL – 26. Statistics: one-way ANOVA Fisher's LSD test.

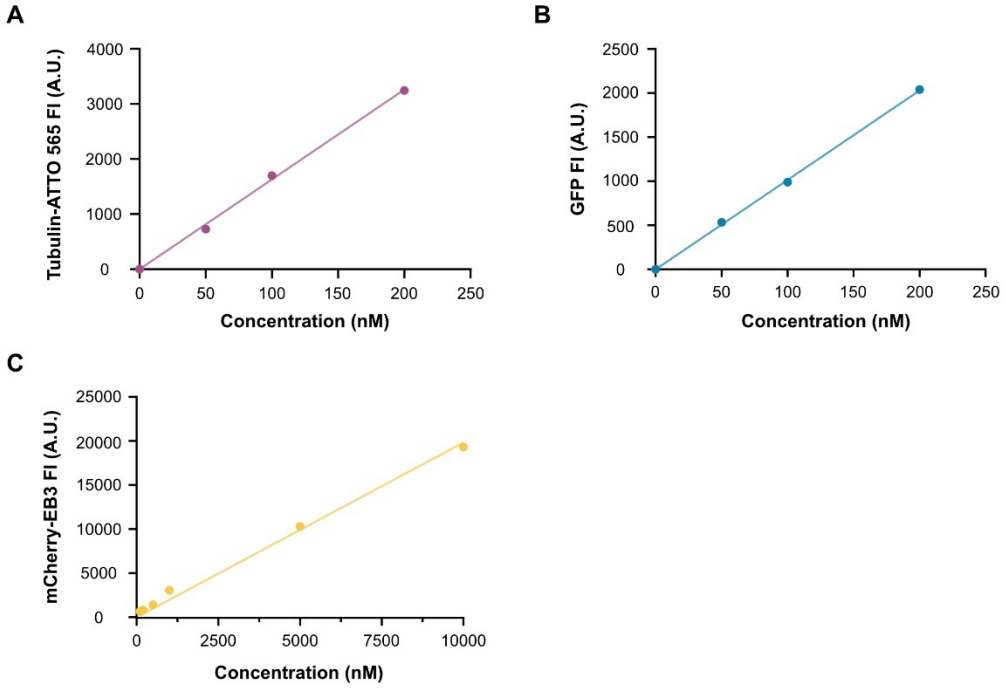

Figure S9: Calibration curve for Tubulin-ATTO 565 , mCherry-EB3 and GFP.

818 Calibration curve between fluorescent intensity and concentration of: (**A**) Tubulin-ATTO 565 at
819 50, 100 and 200 nM. (**B**) GFP at 50, 100 and 200 nM and (**C**) mCherry-EB3 at100, 200, 500, 5
820 000 and 10 000 nM.
821
822
823 **Movie 1**: Representative foci formation resembling fission in GFP-CLIP overexpressing RPE-1
824 cells. Scale bar: 2 µm.
825
826 **Movie 2:** Representative CRISPR/Cas9 knock-in GFP-tubulin RPE-1 expressing mCherry-EB3
827 and treated with 5% 1,6-hexanediol (added at 00:30).
828
829 **Movie 3:** Representative CRISPR/Cas9 knock-in GFP-tubulin RPE-1 expressing mCherry-CLIP.
830 Inset highlights fusion of mCherry-CLIP droplets.
831
832 **Movie 4:** Representative CRISPR/Cas9 knock-in GFP-tubulin RPE-1 expressing mCherry-CLIP.
833 Inset highlights fission of mCherry-CLIP droplets.
834
835 **Movie 5:** Fluorescence recovery after photobleaching of a mCherry-CLIP droplet in a
836 representative CRISPR/Cas9 knock-in GFP-tubulin RPE-1 .
837
838 **Movie 6:** Fusion of two GFP-CLIP droplets (1µM) *in vitro*.
839
840 **Movie 7:** Fluorescence recovery after photobleaching of a purified GFP-CLIP droplet (2 µM) *in*
841 *vitro*.
842
843 **Movie 8:** Representative CRISPR/Cas9 knock-in GFP-tubulin RPE-1 (magenta) expressing
844 mCherry-H1 (cyan).
845
846 **Movie 9:** Representative CRISPR/Cas9 knock-in GFP-tubulin RPE-1 (magenta) expressing
847 mCherry-H2 (cyan).
848
849 **Movie 10:** Fluorescence recovery after photobleaching of a purified EB3 (10 µM) labeled with
850 GFP-EB3 (100 nM) droplet *in vitro*.
851
852 **Movie 11:** Fluorescence recovery after photobleaching of a purified EB3 (10 µM) labeled with
853 GFP-EB3 (100 nM) mixed with GFP-CLIP (2 µM) droplet *in vitro*.
854
855 **Movie 12**: 3D representation of EB3 (8 µM) labelled with mCherry- EB3 (2 µM) droplets *in*
856 *vitro*. Note that floating droplets moved during image acquisition.
857
858 **Movie 13**: 3D representation of GFP-CLIP (2 µM) droplets *in vitro*.
859
860 **Movie 14**: 3D representation of GFP-CLIP (2 µM) mixed with EB3 (8 µM) labelled with
861 mCherry- EB3 (2 µM) droplets *in vitro*. Note that floating droplets moved during image
862 acquisition.
863

864 **Movie 15:** Representative *in vitro* microtubule dynamics assay of Atto-565 tubulin (magenta)
865 polymerized in the presence of 50 nM GFP-FL-CLIP (cyan) and 800 nM EB3 in high salt buffer.
866
867 **Movie 16:** Representative *in vitro* microtubule dynamics assay of Atto-565 tubulin (magenta)
868 polymerized in the presence of 50 nM GFP-FL-CLIP (cyan) and 800 nM EB3 in low salt buffer.
869

870 **Methods**

871 *Cell culture and treatments*

872 Parental RPE1 and CRISPR/Cas9 knock-in RPE1-GFP-tubulin cells were cultured in high glucose
873 Dulbecco's Modified Eagle's Medium F12 (DMEM, ThermoFisher, 113057) supplemented with
874 10 % Fetal Bovine Serum (FBS, ThermoFisher, 10270106) and 1 % penicillin-streptomycin
875 (Gibco, 15140122) at 37°C with 5 % CO_2. The cell lines were monthly checked for mycoplasma
876 contamination. CRISPR/Cas9 knock-in GFP-tubulin RPE-1 cells were generated using the same
877 guide RNA and protocol as in Andreu-Carbó et al., 2022.
878 For transient expression studies of exogenous FL-CLIP, H1, H2 and EB3, cells were transfected
879 using the jetOPTIMUS transfection reagent (Polyplus) with 0.5 µg DNA according to the
880 manufacturer's instructions. Transfection media was replaced with fresh culture media 8 hours
881 post-transfection, and cells were imaged 15-24h after transfection.
882 For experiments in which endogenous CLIP-170 was depleted, parental RPE1 cells were
883 transfected with 10 nM siRNA targeting CLIP-170 (Santa Cruz Biotechnology) using
884 lipofectamine RNAiMAX reagent (Invitrogen) according to the manufacturer's instructions. Media
885 was replaced the following morning, and cells were cultured for 72 hours post-transfection before
886 fixation, or transfected with GFP-H2 24 hours pre-fixation for "knockdown-rescue" experiments
887 with H2. For control experiments, cells were transfected with Allstars Negative Control siRNA
888 (QIAGEN). For CLIP-170 + EB3 depletion experiments, cells were transfected with dual siRNA
889 mixes targeting EB3 (Thermo Fisher, s22683) and CLIP-170 (Santa Cruz, 43281). Transfection
890 media was replaced with fresh culture media 8 hours post-transfection, and cells were imaged 72
891 hours post-transfection.
892 To depolymerize the microtubule network, cells were treated with 5 µM nocodazole (Sigma,
893 M1404; diluted in culture medium) for 1 hour prior to fixation. For experiments using 1,6-
894 hexanediol (Sigma), cells were treated with 5% 1,6-hexanediol (diluted in culture medium) for 10
895 minutes.
896

897 *Cloning*

898 The in-cell expression vector for mCherry-FL-CLIP170 was generated by excising GFP from a
899 GFP-FL-CLIP170 vector (a kind gift from Thomas Surrey) using AgeI/BsrG1 restriction sites and
900 replacing it with mCherry containing AgeI/BsrG1 overhangs generated by PCR. From this vector,
901 we generated mCherry-tagged H1- and H2-CLIP170 by PCR and reinsertion using the XhoI/KpnI
902 restriction sites (N-terminal XhoI primer: 5'-CCGCTCGAGCTCAAGCTTCGATGAGTAT
903 GCTGAAACCCAGCGGGCTGAA-3', C-terminal KpnI H1 primer:
904 5'-CGGGGTACCGTCGACTCAAGTGGTGCCCGAGATCTTGCGGGC-3',
905 and C-terminal KpnI H2 primer: 5'-CGGGGTACCGTCGACTCATTTGTCAGCTTTGGTCTT
906 TTCAAAGAGCAGGCTCTGTTC-3'). Protein purification vectors for GFP-H1- and H2-CLIP
907 were generated by PCR from the GFP-FL-CLIP-170 vector using a primer with an overhang for
908 the NdeI restriction site as well as an N-terminal TEV protease site (5'-
909 GCGGCAGCCATATGGAAAACCTGTATTTCCAGGGAAGTGCCACCATGGTGAGCAAG

910 GGCGAGGAGCTGTTCA-3'), and C-terminal primers specific to each CLIP truncation with
911 overhangs corresponding to the ScaI restriction site (H1: 5'-CCTTATCAAGTACTA
912 GTGGTGCCCGAGATCTTGCGGGCGTAGCGGGAAG-3') (H2: 5'-CCTTATCAAGTACTT
913 CATTTGTCAGCTTTGGTCTTTTCAAAGAGCAGGCTCTGTTCAAGC-3'), then cloned into
914 an empty pET28a-6His vector (a kind gift from Natacha Olieric, Paul Scherrer Institute) using
915 NdeI/ScaI restriction sites.
916
917 For the GFP-H2-tail construct Gilson assembly was used from the GFP-FL-CLIP construct using
918 the primer 5'- CAAGCTTCGAATTCTATGCTGAAACCCAGCGGGCTGAAGG with BstBl
919 (Start of H2), CAGCTCTGCGTCCTTCTCTTTGTCAGCTTTGGTCTTTTCAAAGAGCAG-3'
920 (end of H2), 5'- GCTGACAAAGAGAAGGACGCAGAGCTGGAGAAGCTGAGGAATGAG
921 (start of tail) and CCGCGG TACCGTCGACTCAGAAGGTCTCATCGTCGTTGCAGTTGG
922 (end of tail) using the PKPN enzyme.
923
924 A protein purification vector for mCherry-6His-EB3 was a kind gift from Natacha Olieric (Paul
925 Scherrer Institute). From this vector, mCherry was excised using AgeI/BsrGI restriction sites to
926 produce an untagged 6His-EB3 vector for purification. Mutagenesis of the mCherry-6His-EB3
927 was used to create the EB3-ΔY281, the primer used were 5'-CAAGAAGACCAGGAC
928 GAGTAACAGTAAAGGTGGATAC and GTATCCACCTTTACTGTTACTCGTCCTGGTCTT
929 CTTG-3'.
930 For in-cell expression of EB3, EB3-mCherry vectors were obtained from Addgene (Addgene
931 plasmid 55037).
932
933 *Imaging*
934
935 *Microscope*
936 For in-cell studies and *in vitro* microtubule dynamics experiments, imaging was performed on an
937 Axio Observer Inverted TIRF microscope (Zeiss, 3i) equipped with a Prime 95B BSI
938 (Photometrics) using a 100X objective (Zeiss, Plan-Apochromat 100X/1.46 oil DIC (UV) VIS-
939 IR). SlideBook 6 X 64 software (version 6.0.22) was employed to record time-lapse imaging. For
940 *in vitro* microtubule dynamics and cell imaging, microscope stage conditions were controlled with
941 the Chamlide Live Cell Instrument incubator (37°C for *in vitro* experiments, supplemented with 5
942 % CO_2 for live cell experiments).
943
944 For stack acquisition and intensity measurement a 3i Marianas spinning disk confocal setup based
945 on a Zeiss Z1 stand, a 100× PLAN APO NA 1.45 TIRF objective and a Yokogawa X1 spinning
946 disk head followed by a 1.2× magnification lens and an Evolve EMCCD camera (Photometrics).
947 Fast z-stack acquisition (0.5-µm steps) was obtained using a piezo stage (Mad City Labs). Single-
948 emitter emission filters were always used to avoid bleed-through and each channel was acquired
949 sequentially.
950

951 *Microtubule dynamics*
952 For *in vitro and in cell* microtubule dynamics measurements images were taken every second for
953 3 minutes. Microtubules were tracked individually using the Freehand-Line tool in ImageJ (15-
954 pixel width) and kymographs were built using the KymographBuilder plugin. Microtubule growth
955 speeds were then calculated by manually tracing the slopes of kymographs using the Straight-Line
956 tool in ImageJ and extracting dynamic parameters the slopes using a custom-written code.
957 *Fluorescence recovery after photobleaching*
958 Fluorescence recovery after photobleaching (FRAP) experiments in cells were performed in square
959 regions (4x4 µm) with a 656 nm laser at 20% intensity. The normalized fluorescence intensity was
960 calculated using the formula $F(t)_{norm} = \frac{F(t)_{ROI}-F_{bck}}{F(t)_{ctrl}-F_{bck}} \times \frac{F(i)_{ctrl}-F_{bck}}{F(i)_{ROI}-F_{bck}}$ where $F(t)_{ROI}$ and $F(t)_{ctrl}$ are
961 respectively the ROI and the control fluorescence intensity before the FRAP, F_{bck} the background
962 fluorescence and $F(i)_{ROI}$ and $F(i)_{ctrl}$ are respectively the ROI of the unbleached part of the
963 condensate at one timepoint (i) (Day et al.,2012).
964
965 *+TIP-network analysis in 1,6-hexanediol-treated cells*
966 For experiments in cells treated with 1,6-hexanediol, images were taken in a single z-plane every
967 10 seconds for 10 minutes. 1,6-Hexanediol (5 %) was added after one minute, and cells were only
968 analyzed if they did not undergo any large-scale changes in morphology, as 1,6-hexanediol
969 treatment has been noted to affect mammalian cell shape (Wheeler et al., 2016). For "pre-
970 treatment" time points, all in-focus +TIP-networks on the cell periphery were analyzed in the time
971 frame 10 seconds prior to hexanediol addition using the Segmented-Line tool in ImageJ to obtain
972 fluorescence intensity. For "post-treatment" time points, the same strategy was applied to the time
973 frame 5 minutes after hexanediol addition.
974
975 *Immunofluorescence*
976 15-24 hours post-transfection (or post-seeding for non-transfected cells), cells were fixed with
977 100% methanol for 5 min at -20°C and then for 15 min with 3% paraformaldehyde at room
978 temperature. Cells were then permeabilized for 10 minutes with 0.15% by volume Triton-X 100
979 (Sigma) in PBS followed by 10 minutes with 0.1% Tween-20 (AppliChem) in PBS, washed
980 thoroughly in a solution of 0.05% Tween-20 in PBS (hereafter referred to as PBS-T), and
981 subsequently blocked with 2% bovine serum albumin (in PBS) for 1h. Post-blocking, cells were
982 incubated overnight with antibodies targeting tubulin (Sigma T6199, DM1α, 1:1000, mouse), EB1
983 (Millipore AB 6057, rabbit, 1:1000), EB3 (Santa Cruz Biotechnology sc-101475, KT36, rat,
984 1:200), or CLIP-170 (Santa Cruz Biotechnology sc-28325, F3, mouse, 1:500). Primary antibodies
985 were diluted to the appropriate concentration in 2% bovine serum albumin in PBS. The following
986 day, cells were subjected to three five-minute washes at room temperature in PBS-T, then
987 subsequently incubated in secondary antibodies (Invitrogen, species-specific IgG conjugated to
988 Alexa-647, 568, or 488 fluorophores) at room temperature for one hour. Cells were subjected to
989 three additional PBS-T washes, and coverslips were mounted onto glass microscopy slides (Glass

990 technology) using ProLong™ Diamont Antifade Mountant. Coverslips were sealed with nail
991 polish and stored at 4°C until imaging.
992
993 *Tubulin purification from bovine brain and labelling*
994 Tubulin was purified from fresh bovine brain by two subsequent polymerization/depolymerization
995 cycles as described previously (Andreu-Carbó et al., 2022). Tubulin labelling with biotin or
996 ATTO-488, -565, -647 fluorophores was performed as described (Andreu-Carbó et al., 2022), and
997 final labelling ratios to polymerize microtubules were 11% for ATTO-488 and 13% for ATTO-
998 565 tubulin.
999
1000 *Protein purification*
1001 For purification of EB3, mCherry-EB3, EB3-ΔY and mCherry-EB3-ΔY, *E. coli* BL21 (DE3) cells
1002 were transformed with 6-His-tagged EB3-encoding plasmids and induced for expression overnight
1003 with 1 mM IPTG at 20°C under rotation at 200 rpm. All following steps were performed at 4°C.
1004 The morning after induction, cells were lysed by in lysis buffer (20 mM Tris pH 7.5, 300 mM
1005 NaCl) supplemented with 1% Triton-X 100 and protease inhibitors cocktail tablets (Roche) and
1006 sonicated. Cell debris were then cleared by ultracentrifugation. The cleared lysate was
1007 subsequently loaded onto a pre-equilibrated HisTrap column (GE Healthcare 1mL HisTrap
1008 column) using an ÄKTA Pure Protein Purification System (GE Healthcare). After washing the
1009 column in lysis buffer, elution buffer (20 mM Tris pH 7.5, 300 mM NaCl, 1 M imidazole) was
1010 applied to the column in a 1% gradient. Eluted protein fractions were pooled and concentrated
1011 using Amicon 30K Centrifugal filters (Millipore). The concentrated, cleared protein was subjected
1012 to size-exclusion chromatography using a HiLoad 16/600 Superdex column (GE Healthcare) in
1013 lysis buffer. Protein-containing fractions were harvested, pooled, and concentrated. Protein was
1014 supplemented with 20% glycerol, aliquoted, snap-frozen and stored at -80°C.
1015 GFP-H1, GFP-H2 and GFP-H2-tail were purified using the same scheme as EB3, with the
1016 following differences: (1) the lysis buffer was 50 mM potassium phosphate pH 7.5, 500 mM NaCl,
1017 1 mM $MgCl_2$, and 1 mM β-mercaptoethanol. (2) Between applying protein to the HisTrap column
1018 and elution, the column was washed with lysis buffer supplemented with 8 mM Imidazole. (3) H1-
1019 and H2-CLIP were eluted from the HisTrap column using lysis buffer + 300 mM Imidazole, and
1020 protein-containing fractions were subjected to tobacco etch virus (TEV) protease treatment
1021 overnight to remove His tags prior to size-exclusion chromatography.
1022 FL-CLIP170-GFP was purified from insect cells as described previously (Telley et al., 2011). A
1023 plasmid encoding FL-CLIP170-GFP in pFasBacHTa (a kind gift from Thomas Surrey) was used
1024 to generate Baculovirus, which was subsequently used to infect Sf9 cells. Cells were harvested
1025 and lysed with lysis buffer (30 mM HEPES pH 7.4, 400 mM KCl, 20 mM Arginine, 20 mM
1026 potassium-glutamate, 0.01% Birj35, 2 mM $MgCl_2$, 10 mM β-mercaptoethanol) supplemented with
1027 20 mM imidazole and protease inhibitor tablets (Roche) using dounce homogenization. Cell debris
1028 were cleared by ultracentrifugation, and cleared lysate was loaded onto a Histrap column (GE
1029 Healthcare). The column was washed with lysis buffer supplemented with 50 mM imidazole, then

1030 eluted with lysis buffer supplemented with 300 mM imidazole. Protein-containing fractions were
1031 pooled and further cleared by a second centrifugation, then subjected to size-exclusion
1032 chromatography using a HiLoad 16/600 Superdex column (GE Healthcare) in lysis buffer (lacking
1033 Birj35). Only proteins coming off with a clean, single peak profile from the Superdex column were
1034 used. Protein-containing fractions were pooled and concentrated and used immediately (maximal
1035 5 hrs after purification), as FL-CLIP was prone to degradation and loss of activity after freezing
1036 as previously noted (Telley et al., 2011). For all purified proteins, protein concentration was
1037 measured by Bradford assay.
1038
1039 *Phase separation assay*
1040 For in vitro phase separation assays, proteins were diluted to the appropriate concentration in
1041 BRB80 supplemented with 50 mM potassium chloride and PEG 4000 (0, 2, 5 or 10 % by weight)
1042 in Eppendorf tubes. After thorough mixing, reactions were transferred to 384-well plates (Falcon)
1043 and incubated for 7 min. The plate was then centrifuged at 2000 rpm for 1 min to sediment proteins
1044 in the dense phase on the well bottoms. Images were acquired using a confocal automated
1045 microscope (Molecular Device) with a 60X dry objective. For each reaction, 9 times 2048 x 2048
1046 px fields of view were acquired with one focal plane (Figure S1A). Automated analysis was
1047 performed using MetaXpress Custom Module editor software. From fluorescence intensity, masks
1048 were generated to differentiate condensates from the background and the area sum was calculated
1049 together with the condensate versus background fluorescence intensity.
1050
1051 *Droplet-Pelleting assay*
1052 For the droplet-pelleting assays to determine amount of protein in the dense phase (Figure 5A)
1053 proteins were diluted to the appropriate concentrations (1 µM CLIP, 10 µM EB3, or 1 µM CLIP
1054 + 10 µM EB3) in BRB supplemented with 125 mM potassium chloride and incubated at room
1055 temperature for 30 minutes. Following this incubation, reaction mixtures were centrifuged at
1056 16,900 g at room temperature for 15 minutes using a Fresco 21 Haraeus tabletop centrifuge
1057 (Thermo Scientific). The supernatant was collected, and pellets were resuspended in an equal
1058 volume of resuspension buffer (BRB80 + 125 mM KCl). Pellets and supernatants from each
1059 reaction were run on SDS-PAGE gels, which were subsequently stained with QuickBlue Protein
1060 Stain Coomassie dye (Lubio Science) for at least 2 hours before destaining in water. The fraction
1061 of protein in dense vs dilute phase was calculated by dividing the integrated Coomassie band
1062 intensity from the pellet or supernatant, respectively, by the sum of the integrated band intensity
1063 of the pellet and supernatant. Fold-change in pellet fraction was taken by dividing the protein
1064 fraction in the pellet for experiments with CLIP + EB3 by the protein fraction in the pellet for each
1065 protein alone.
1066
1067 *Fixation of FL-CLIP droplets*
1068 For experiments in which FL-CLIP droplets were fixed to observe whether unlabeled tubulin
1069 partitions into droplets (Figure S6B), GFP-CLIP (200 nM) was incubated with unlabeled purified

1070 bovine brain tubulin (400 nM) on coverslips for 15 minutes. Reactions were fixed directly on
1071 coverslips with 3% PFA for 15 minutes, washed 3 times in PBS, blocked and stained with
1072 antibodies to tubulin as described in the above immunofluorescence procedure.
1073
1074 *Calibration curve*
1075 To measure the concentration of proteins in the dilute and in the droplet phase, calibration curves
1076 were established for GFP, tubulin-565 and mCherry-EB3. To avoid mCherry-EB3 phase
1077 separation a buffer with 1M NaCl was used. To establish the curve the following concentrations
1078 were used: GFP (50, 100 and 200 nM); mCherry-EB3 (100, 200, 500, 5 000 and 10 000 nM); and
1079 tubulin (50, 100 and 200 nM).
1080
1081 *Coverslip treatment and Flow chamber preparation*
1082 For *in vitro* microtubule dynamics studies, slides and coverslips were cleaned by two successive
1083 30-minute sonication cycles in 1 M NaOH followed by 96% ethanol with thorough rinsing in bi-
1084 distilled water between each step. After drying, slides and coverslips were plasma treated
1085 (Electronic Diener, Plasma surface technology) and subsequently incubated for 48 hours with tri-
1086 ethoxy-silane-PEG (Creative PEGWorks) or a 1:5 mix of tri-ethoxy-silane-PEG-biotin: tri-ethoxy-
1087 silane-PEG (final concentration 1 mg/ml) in 96 % ethanol and 0.02 % HCl, with gentle agitation
1088 at room temperature. Slides and coverslips were then washed in ethanol (96 %) followed by
1089 thorough washing in bi-distilled water, then dried with an air gun and stored at 4°C. Flow chambers
1090 were prepared by affixing a silane-PEG-biotin coverslip to a silane-PEG slide using double-sided
1091 tape.
1092
1093 *Microtubule dynamics assays in vitro*
1094 Microtubule seeds were prepared at a final concentration of 10 µM tubulin (20 % ATTO-647-
1095 labelled tubulin and 80 % biotinylated tubulin) in BRB80 supplemented with 0.5 mM GMPCPP
1096 (Jena Bioscience) for 45 minutes at 37°C. Seeds were incubated with 1 µM Paclitaxel (Sigma) for
1097 45 minutes at 37°C, centrifuged (50,000 rpm at 37°C for 15 min), resuspended in BRB80
1098 supplemented with 1 µM Paclitaxel and 0.5 mM GMPCPP, aliquoted and subsequently stored in
1099 liquid nitrogen.
1100 Flow chambers were prepared by injecting subsequently 50 µg/mL neutravidin (ThermoFisher),
1101 BRB80, and microtubule seeds, then subsequently washing out unattached seeds with BRB80.
1102 Reaction buffer containing Atto-565 labelled-tubulin (1:5 ratio labelled to unlabeled; 5 µM for all
1103 assays except for Figure S6B, C) in BRB80 supplemented with an anti-bleaching buffer [10 mM
1104 DTT, 0.3 mg/mL glucose, 0.1 mg/mL glucose oxidase, 0.02 mg/mL catalase, 0.125 % methyl
1105 cellulose (1500 cP, Sigma), 1 mM GTP] was subsequently injected, and chambers were sealed
1106 with silicon grease and immediately imaged. For "low salt" assays (Figure 6E-F), the reaction
1107 buffer was supplemented with 60 mM potassium chloride. For "high salt" assays (Figure 6A-B),
1108 the reaction buffer was supplemented with 60 mM potassium chloride and 85 mM potassium
1109 acetate to facilitate tip tracking as described previously (Telley et al., 2011).

1110 For assays involving recombinant EB3 and H1- or H2-CLIP-170, purified proteins were flash-
1111 thawed and spun at 50,000 rpm in a TLA-100 centrifuge at 4°C for 15 minutes to remove any large
1112 aggregates. Proteins were diluted into BRB80 immediately prior to their usage, and further diluted
1113 to the appropriate concentration in reaction buffer. Assays involving FL-CLIP-170 were carried
1114 out as noted above, but within the first 5 hours post-purification as FL-CLIP-170 activity is poorly
1115 preserved after freezing (Telley et al., 2011).
1116
1117 *Comparison between mCherry- and GFP-CLIP expression vs condensation phenotypes*
1118 Cells were plated on 96 well plates and transfected using the TransIT-X2 (Mirus) transfection
1119 reagent with 0.075 µg DNA per well according to the manufacturer's instructions**.** Images were
1120 acquired using a confocal automated microscope (Molecular Device) with a 60X water objective.
1121 The first 100 cells observed for each experiment were binned according to their condensation
1122 phenotype, as detailed in Figure S2A and B.
1123
1124 *SDS-PAGE and Western blot*
1125 Purified proteins or cell lysates were boiled, diluted into sample buffer containing Coomassie dye
1126 and x % SDS, and run on gels containing 10% Agarose. After protein separation, gels were stained
1127 with QuickBlue Protein Stain Coomassie dye (Lubio Science) for at least 2 hours before destaining
1128 in water.
1129 Cell lysates were boiled run on SDS-PAGE gels (10% acrylamide) and subsequently transferred
1130 to a nitrocellulose membrane using an iBLOT 2 Gel Transfer Device (ThermoFisher Scientific,
1131 IB21001). Nitrocellulose membranes were blocked for 1 h with 5 % dried milk resuspended in
1132 TBS-Tween 1 %, then incubated over-night with primary antibodies: anti-beta-tubulin (Sigma,
1133 T6074, 1:1000 dilution) anti-EB3 (ATLAS anti-MAPRE3, HPA-009263, 1:500 dilution), or anti-
1134 CLIP-170 (Santa Cruz Biotechnology, SC-28325, 1:1000 dilution). The following day, unbound
1135 antibodies were washed off with TBS-Tween 1%, and membranes were incubated with secondary
1136 antibodies conjugated to horseradish peroxidase (anti-mouse or anti-rabbit; GE Healthcare
1137 17097199 and 16951542, 1:5000 dilution) for 1 hour at room temperature. Following secondary
1138 antibody incubation, membranes were washed extensively with TBS-Tween 1% and imaged using
1139 an ECL Western blotting detection kit (Advansta) and with Fusion Solo Vilber Lourmat camera
1140 (Witec ag).
1141
1142 *Statistical analysis*
1143 Statistical analyses were carried out using GraphPad Prism software v9 as described in figure
1144 legends. Unless otherwise noted, analyses were carried out between experimental means using
1145 one-way ANOVA Fisher's LSD test, or two-tailed Student's t-test. P-values less than 0.05 were
1146 considered statistically significant.
1147
1148 **References**
1149

Akhmanova, A., & Steinmetz, M. O. (2010). Microtubule +TIPs at a glance. J Cell Sci, 123(Pt 20), 3415-3419. https://doi.org/10.1242/jcs.062414

Akhmanova, A., & Steinmetz, M. O. (2015). Control of microtubule organization and dynamics: two ends in the limelight. Nat Rev Mol Cell Biol, 16(12), 711-726. https://doi.org/10.1038/nrm4084

Alberti, S., & Dormann, D. (2019). Liquid–Liquid Phase Separation in Disease. Annual Review of Genetics, 53(1), 171-194. https://doi.org/10.1146/annurev-genet-112618-043527

Andreu-Carbó M., Fernandes S., Velluz M. C., Kruse K., Aumeier C. (2022). Motor usage imprints microtubule stability along the shaft. Dev Cell, 57(1):5-18.e8. doi: https://doi.org/10.1016/j.devcel.2021.11.019

Arnal, I., Heichette, C., Diamantopoulos, G. S., & Chretien, D. (2004). CLIP-170/tubulin-curved oligomers coassemble at microtubule ends and promote rescues. Curr Biol, 14(23), 2086-2095. https://doi.org/10.1016/j.cub.2004.11.055

Bieling P., Laan L., Schek H., Munteanu E. L., Sandblad L., Dogterom M., Brunner D., Surrey T. (2007). Reconstitution of a microtubule plus-end tracking system in vitro. Nature, 13;450(7172):1100-5. https://doi.org/10.1038/nature06386

Bieling P., Kandels-Lewis S., Telley I. A., van Dijk J., Janke, C., & Surrey, T. (2008). CLIP-170 tracks growing microtubule ends by dynamically recognizing composite EB1/tubulin-binding sites. J Cell Biol, 183(7), 1223-1233. https://doi.org/10.1083/jcb.200809190

Bjelić S., De Groot C. O., Schärer M. A., Jaussi R., Bargsten K., Salzmann M., Frey D., Capitani G., Kammerer R. A., Steinmetz M. O. (2012). Interaction of mammalian end binding proteins with CAP-Gly domains of CLIP-170 and p150(glued). J Struct Biol, 177(1):160-7. https://doi.org/10.1016/j.jsb.2011.11.010

Boeynaems, S., Alberti, S., Fawzi, N. L., Mittag, T., Polymenidou, M., Rousseau, F., Schymkowitz, J., Shorter, J., Wolozin, B., Van Den Bosch, L., Tompa, P., & Fuxreiter, M. (2018). Protein Phase Separation: A New Phase in Cell Biology. Trends Cell Biol, 28(6), 420-435. https://doi.org/10.1016/j.tcb.2018.02.004

Brouhard, G. J. (2015). Dynamic instability 30 years later: complexities in microtubule growth and catastrophe. Mol Biol Cell. 26(7), 1207-1210. https://doi.org/10.1091/mbc.E13-10-0594

Brouhard, G. J., & Rice, L. M. (2018). Microtubule dynamics: an interplay of biochemistry and mechanics. Nat Rev Mol Cell Biol, 19(7), 451-463. https://doi.org/10.1038/s41580-018-0009-y

Brouhard, G. J., Stear, J. H., Noetzel, T. L., Al-Bassam, J., Kinoshita, K., Harrison, S. C., Howard, J., & Hyman, A. A. (2008). XMAP215 is a processive microtubule polymerase. Cell, 132(1), 79-88. https://doi.org/10.1016/j.cell.2007.11.043

1194 Chen, J., Kholina, E., Szyk, A., Fedorov, V. A., Kovalenko, I., Gudimchuk, N., & Roll-Mecak,
1195 A. (2021). alpha-tubulin tail modifications regulate microtubule stability through selective
1196 effector recruitment, not changes in intrinsic polymer dynamics. Dev Cell.
1197 https://doi.org/10.1016/j.devcel.2021.05.005
1198
1199 De Forges, H., Pilon, A., Cantaloube, I., Pallandre, A., Haghiri-Gosnet, A., Perez, F., and Poüs,
1200 C. (2016). Localized Mechanical Stress Promotes Microtubule Rescue. Current Biology 2016
1201 Dec 19; 26(24) 3399-3406. https://doi.org/10.1016/j.cub.2016.10.048
1202
1203 Diamantopoulos, G. S., Perez, F., Goodson, H. V., Batelier, G., Melki, R., Kreis, T. E., &
1204 Rickard, J. E. (1999). Dynamic localization of CLIP-170 to microtubule plus ends is coupled to
1205 microtubule assembly. J Cell Biol, 144(1), 99-112. https://doi.org/10.1083/jcb.144.1.99
1206
1207 Dixit, R., Barnett, B., Lazarus, J. E., Tokito, M., Goldman, Y. E., & Holzbaur, E. L. (2009).
1208 Microtubule plus-end tracking by CLIP-170 requires EB1. Proc Natl Acad Sci U S A, 106(2),
1209 492-497. https://doi.org/10.1073/pnas.0807614106
1210
1211 Drechsel D.N., and Kirschner M. W. (1994) The minimum GTP cap required to stabilize
1212 microtubules. Curr Biol, 1;4(12):1053-61. https://doi.org/10.1016/s0960-9822(00)00243-8.
1213
1214 Duellberg, C., Trokter, M., Jha, R., Sen, I., Steinmetz, M. O., & Surrey, T. (2014).
1215 Reconstitution of a hierarchical +TIP interaction network controlling microtubule end tracking of
1216 dynein. Nat Cell Biol, 16(8), 804-811. https://doi.org/10.1038/ncb2999
1217
1218 Folker, E. S., Baker, B. M., and Goodson, H. V. (2005) Interactions between CLIP-170, tubulin,
1219 and microtubules: implications for the mechanism of Clip-170 plus-end tracking behavior. Mol
1220 Biol Cell 2005 Nov; 16(11):5373-84. https://doi.org/10.1091/mbc.e04-12-1106
1221
1222 Ford, L. K., and Fioriti, L. (2020) Coiled-Coil Motifs of RNA-Binding Proteins: Dynamicity in
1223 RNA Regulation. Front Cell Dev Biol. https://doi.org/10.3389/fcell.2020.607947
1224
1225 Galjart, N. (2010). Plus-end-tracking proteins and their interactions at microtubule ends. Curr
1226 Biol, 20(12), R528-537. https://doi.org/10.1016/j.cub.2010.05.022
1227
1228 Gard, D. L., & Kirschner, M. W. (1987). A microtubule-associated protein from Xenopus eggs
1229 that specifically promotes assembly at the plus-end. J Cell Biol, 105(5), 2203-2215.
1230 https://doi.org/10.1083/jcb.105.5.2203
1231
1232 Goodson, H. V., Skube, S. B., Stalder, R., Valetti, C., Kreis, T. E., Morrison, E. E., & Schroer, T.
1233 A. (2003). CLIP-170 interacts with dynactin complex and the APC-binding protein EB1 by
1234 different mechanisms. Cell Motil Cytoskeleton, 55(3), 156-173.
1235 https://doi.org/10.1002/cm.10114
1236
1237 Gudimchuk N. B., & McIntosh J. R. (2021). Regulation of microtubule dynamics, mechanics and
1238 function through the growing tip. Nat Rev Mol Cell Biol. 22(12):777-795.
1239 https://doi.org/10.1038/s41580-021-00399-x

Gupta, K. K., Joyce, M. V., Slabbekoorn, A. R., Zhu, Z. C., Paulson, B. A., Boggess, B., & Goodson, H. V. (2010). Probing interactions between CLIP-170, EB1, and microtubules. J Mol Biol, 395(5), 1049-1062. https://doi.org/10.1016/j.jmb.2009.11.014

Henrie, H., Bakhos-Douaihy, D., Cantaloube, I., Pilon, A., Talantikite, M., Stoppin-Mellet, V., Baillet, A., Pous, C., & Benoit, B. (2020). Stress-induced phosphorylation of CLIP-170 by JNK promotes microtubule rescue. J Cell Biol, 219(7). https://doi.org/10.1083/jcb.201909093

Hernandez-Vega, A., Braun, M., Scharrel, L., Jahnel, M., Wegmann, S., Hyman, B. T., Alberti, S., Diez, S., & Hyman, A. A. (2017). Local Nucleation of Microtubule Bundles through Tubulin Concentration into a Condensed Tau Phase. Cell Rep, 20(10), 2304-2312. https://doi.org/10.1016/j.celrep.2017.08.042

Howard, J., & Hyman, A. A. (2009). Growth, fluctuation and switching at microtubule plus ends. Nat Rev Mol Cell Biol, 10(8), 569-574. https://doi.org/10.1038/nrm2713

Hyman AA, Weber CA, Jülicher F. Liquid-liquid phase separation in biology. Annu Rev Cell Dev Biol. 2014;30:39-58. https://doi.org/10.1146/annurev-cellbio-100913-013325

Jiang, H., Wang, S., Huang, Y., He, X., Cui, H., Zhu, X., & Zheng, Y. (2015). Phase transition of spindle-associated protein regulate spindle apparatus assembly. Cell, 163(1), 108-122. https://doi.org/10.1016/j.cell.2015.08.010

Jiang, X., Ho, D. B. T., Mahe, K., Mia, J., Sepulveda, G., Antkowiak, M., Jiang, L., Yamada, S., & Jao, L. E. (2021). Condensation of pericentrin proteins in human cells illuminates phase separation in centrosome assembly. J Cell Sci. https://doi.org/10.1242/jcs.258897

Jijumon, A. S., Bodakuntla, S., Genova, M., Bangera, M., Sackett, V., Besse, L., Maksut, F., Henriot, V., Magiera, M. M., Sirajuddin, M., and Janke, C. (2022). Lysate-based pipeline to characterize microtubule-associated proteins uncovers unique microtubule behaviors. Nat Cell Bio 24, 253-267. https://doi.org/10.1038/s41556-021-00825-4

King, M. R., & Petry, S. (2020). Phase separation of TPX2 enhances and spatially coordinates microtubule nucleation. Nat Commun, 11(1), 270. https://doi.org/10.1038/s41467-019-14087-0

Komarova, Y., De Groot, C. O., Grigoriev, I., Gouveia, S. M., Munteanu, E. L., Schober, J. M., Honnappa, S., Buey, R. M., Hoogenraad, C. C., Dogterom, M., Borisy, G. G., Steinmetz, M. O., & Akhmanova, A. (2009). Mammalian end binding proteins control persistent microtubule growth. J Cell Biol, 184(5), 691-706. https://doi.org/10.1083/jcb.200807179

Komarova, Y., Lansbergen, G., Galjart, N., Grosveld, F., Borisy, G. G., & Akhmanova, A. (2005). EB1 and EB3 control CLIP dissociation from the ends of growing microtubules. Mol Biol Cell, 16(11), 5334-5345. https://doi.org/10.1091/mbc.e05-07-0614

1285 Komarova, Y. A., Akhmanova, A. S., Kojima, S., Galjart, N., & Borisy, G. G. (2002).
1286 Cytoplasmic linker proteins promote microtubule rescue in vivo. J Cell Biol, 159(4), 589-599.
1287 https://doi.org/10.1083/jcb.200208058
1288
1289 Kroschwald, S., Maharana, S., & Simon, A. (2017). Hexanediol: a chemical probe to investigate
1290 the material properties of membrane-less compartments.
1291 https://doi.org/10.19185/MATTERS.201702000010
1292
1293 Larson A. G., Elnatan D., Keenen M. M., Trnka M. J., Johnston J. B., Burlingame A. L., Agard
1294 D. A., Redding S., Narlikar G. J. (2017). Liquid droplet formation by HP1α suggests a role for
1295 phase separation in heterochromatin. Nature, 547(7662):236-240.
1296 https://doi.org/10.1038/nature22822
1297
1298 Maan, R., Reese, L., Volkov, V. A., King, M. R., van der Sluis, E., Andrea., N., Evers, W.,
1299 Jakobi, A. J., and Dogterom, M. (2021). Multivalent interactions facilitate motor-dependent
1300 protein accumulation at growing microtubule plus ends. Biorxiv.
1301 https://doi.org/10.1101/2021.09.14.460284
1302
1303 Meier., S. A., Farcas, A., Kumar, A., Ijavi, M., Bill., R. T., Stelling, J., Dufresne, E., Steinmetz,
1304 M. O., and Barral, Y. (2021). High interaction valency ensures cohesion and persistence of a
1305 microtubule +TIP body at the plus-end of a single specialized microtubule in yeast. Biorxiv.
1306 https://doi.org/10.1101/2021.09.13.460064
1307
1308 Mészáros B., Erdos G., Dosztányi Z. (2018). IUPred2A: context-dependent prediction of protein
1309 disorder as a function of redox state and protein binding. Nucleic Acids Res, 2;46(W1):W329-
1310 W337. https://doi.org/10.1093/nar/gky384
1311
1312 Mitrea, D. M., and Kriwacki, R. W. (2016) Phase separation in biology; functional organization
1313 of a higher order. Cell Commun Signal 14 (1). https://doi.org/10.1186/s12964-015-0125-7
1314
1315 Mohan R., Katrukha E. A., Doodhi H., Smal I., Meijering E., Kapitein L. C., Steinmetz M. O.,
1316 Akhmanova A. (2013) End-binding proteins sensitize microtubules to the action of microtubule-
1317 targeting agents. Proc Natl Acad Sci U S A. 28;110(22):8900-5.
1318 https://doi.org/10.1073/pnas.1300395110
1319
1320 Montenegro Gouveia, S., Leslie, K., Kapitein, L. C., Buey, R. M., Grigoriev, I., Wagenbach, M.,
1321 Smal, I., Meijering, E., Hoogenraad, C. C., Wordeman, L., Steinmetz, M. O., & Akhmanova, A.
1322 (2010). In vitro reconstitution of the functional interplay between MCAK and EB3 at
1323 microtubule plus ends. Curr Biol, 20(19), 1717-1722. https://doi.org/10.1016/j.cub.2010.08.020
1324
1325 Mustyatsa, V. V., Kostarev, A. V., Tvorogova, A. V., Ataullakhanov, F. I., Gudimchuk, N. B., &
1326 Vorobjev, I. A. (2019). Fine structure and dynamics of EB3 binding zones on microtubules in
1327 fibroblast cells. Mol Biol Cell, 30(17), 2105-2114. https://doi.org/10.1091/mbc.E18-11-0723
1328
1329 Nakamura S., Grigoriev I., Nogi T., Hamaji T., Cassimeris L., Mimori-Kiyosue Y. (2012).
1330 Dissecting the nanoscale distributions and functions of microtubule-end-binding proteins EB1

and ch-TOG in interphase HeLa cells. PLoS One. 7(12):e51442. https://doi.org/10.1371/journal.pone.0051442

Perez, F., Diamantopoulos, G. S., Stalder, R., & Kreis, T. E. (1999). CLIP-170 highlights growing microtubule ends in vivo. Cell, 96(4), 517-527. https://doi.org/10.1016/s0092-8674(00)80656-x

Pierre, P., Pepperkok, R., & Kreis, T. E. (1994). Molecular characterization of two functional domains of CLIP-170 in vivo. J Cell Sci, 107 (Pt 7), 1909-1920. https://www.ncbi.nlm.nih.gov/pubmed/7983157

Pierre, P., Scheel, J., Rickard, J. E., & Kreis, T. E. (1992). CLIP-170 links endocytic vesicles to microtubules. Cell, 70(6), 887-900. https://doi.org/10.1016/0092-8674(92)90240-d

Rickman, J., Duellberg, C., Cade, C. I., Griffin, L. D., and Surrey, T. (2017). Steady-state EB cap size fluctuations are determined by stochastic microtubule growth and maturation. PNAS, 2017 March 28; 114 (13): 3427-3432. https://doi.org/10.1073/pnas.1620274114

Roth D., Fitton B. P., Chmel N. P., Wasiluk N., Straube A. (2018). Spatial positioning of EB family proteins at microtubule tips involves distinct nucleotide-dependent binding properties. J Cell Sci, 132(4):jcs219550. https://doi.org/10.1242/jcs.219550

Salisbury, S. (2003). Centrosomes: Coiled-Coils Organize the Cell Center. Current Biology 13 (3):88-90. https://doi.org/10.1016/S0960-9822(03)00033-2

Schek III, H. T., Gardner, M. K., Cheng, J., Odde, D. J., and Hunt, A. J. (2007). Microtubule Assembly Dynamics at the Nanoscale. Current Biology 17 (17): 1445-1455. https://doi.org/10.1016/j.cub.2007.07.011

Seetapun D, Castle BT, McIntyre AJ, Tran PT, Odde DJ. Estimating the microtubule GTP cap size in vivo. Curr Biol. 2012 Sep 25;22(18):1681-7. https://doi.org/10.1016/j.cub.2012.06.068

Shin Y, Brangwynne CP. Liquid phase condensation in cell physiology and disease. Science. 2017 Sep 22;357(6357):eaaf4382. https://doi.org/10.1126/science.aaf4382

Song et al., 2022 (personal communications)

Srayko, M., Kaya, A., Stamford, J., & Hyman, A. A. (2005). Identification and characterization of factors required for microtubule growth and nucleation in the early C. elegans embryo. Dev Cell, 9(2), 223-236. https://doi.org/10.1016/j.devcel.2005.07.003

Strom A. R., Emelyanov A. V., Mir M., Fyodorov D. V., Darzacq X., Karpen G. H. (2017). Phase separation drives heterochromatin domain formation. 13;547(7662):241-245. https://doi.org/10.1038/nature22989

1377 Straube, A., & Merdes, A. (2007). EB3 regulates microtubule dynamics at the cell cortex and is
1378 required for myoblast elongation and fusion. Curr Biol, 17(15), 1318-1325.
1379 https://doi.org/10.1016/j.cub.2007.06.058
1380
1381 Telley, I. A., Bieling, P., & Surrey, T. (2011). Reconstitution and quantification of dynamic
1382 microtubule end tracking in vitro using TIRF microscopy. Methods Mol Biol, 777, 127-145.
1383 https://doi.org/10.1007/978-1-61779-252-6_10
1384
1385 Vitre, B., Coquelle, F. M., Heichette, C., Garnier, C., Chretien, D., & Arnal, I. (2008). EB1
1386 regulates microtubule dynamics and tubulin sheet closure in vitro. Nat Cell Biol, 10(4), 415-421.
1387 https://doi.org/10.1038/ncb1703
1388
1389 Voter, W. A., O'Brien, E. T., & Erickson, H. P. (1991). Dilution-induced disassembly of
1390 microtubules: relation to dynamic instability and the GTP cap. Cell Motil Cytoskeleton, 18(1),
1391 55-62. https://doi.org/10.1002/cm.970180106
1392
1393 Walker, R. A., O'Brien, E. T., Pryer, N. K., Soboeiro, M. F., Voter, W. A., Erickson, H. P., &
1394 Salmon, E. D. (1988). Dynamic instability of individual microtubules analyzed by video light
1395 microscopy: rate constants and transition frequencies. J Cell Biol, 107(4), 1437-1448.
1396 https://doi.org/10.1083/jcb.107.4.1437
1397
1398 Wiśniewski, J. R., Hein, M. Y., Cox, J., and Mann, M. (2014). A "Proteomic Ruler" for Protein
1399 Copy Number and Concentration Estimation without Spike-in Standards. Molecular & Cellular
1400 Proteomics 13(12):3497-3506. https://doi.org/10.1074/mcp.M113.037309
1401
1402 Woodruff, J. B., Ferreira Gomes, B., Widlund, P. O., Mahamid, J., Honigmann, A., & Hyman,
1403 A. A. (2017). The Centrosome Is a Selective Condensate that Nucleates Microtubules by
1404 Concentrating Tubulin. Cell, 169(6), 1066-1077 e1010.
1405 https://doi.org/10.1016/j.cell.2017.05.028
1406
1407 Wu, Y.-F. O., Bryant, A. T., Nelson, N. T., Madey, A. G., Fernandes, G. F., & Goodson, H. V.
1408 (2021). Overexpression of the microtubule-binding protein CLIP-170 induces a +TIP network
1409 superstructure consistent with a biomolecular condensate. PLoS One, 10;16(12):e0260401.
1410 https://doi.org/10.1371/journal.pone.0260401.
1411
1412 Yang, C., Wu, J., de Heus, C., Grigoriev, I., Liv, N., Yao, Y., Smal, I., Meijering, E.,
1413 Klumperman, J., Qi, R. Z., & Akhmanova, A. (2017). EB1 and EB3 regulate microtubule minus
1414 end organization and Golgi morphology. J Cell Biol, 216(10), 3179-3198.
1415 https://doi.org/10.1083/jcb.201701024
1416
1417 Zanic, M., Widlund, P. O., Hyman, A. A., & Howard, J. (2013). Synergy between XMAP215
1418 and EB1 increases microtubule growth rates to physiological levels. Nat Cell Biol, 15(6), 688-
1419 693. https://doi.org/10.1038/ncb2744
1420

Zhang R., Alushin G. M., Brown A., Nogales E. (2015). Mechanistic Origin of Microtubule Dynamic Instability and Its Modulation by EB Proteins. Cell, 13;162(4):849-59. doi: https://doi.org/10.1016/j.cell.2015.07.012